Applications in Energy and Combustion Science 7 (2021) 100037

Contents lists available at ScienceDirect

Applications in Energy and Combustion Science

journal homepage: www.sciencedirect.com/journal/applications-in-energy-and-combustion-science

Simulation of transient effects in a fuel injector nozzle using real-fluid thermodynamic closure

Konstantinos Kolovos [1,*], Nikolas Kyriazis [2], Phoevos Koukouvinis [2], Alvaro Vidal [2], Manolis Gavaises [2], Robert M. McDavid [3]

[1] Perkins Engines Company Ltd, Peterborough, PE1 5NA, United Kingdom
[2] City University London, Northampton Square EC1V 0HB, United Kingdom
[3] Caterpillar Inc, Mossville, IL 61552, United States

ARTICLE INFO

Keywords:
Cavitation
real-fluid
erosion
X-rays
explicit density-based solver
LES
ALE

ABSTRACT

Numerical predictions of the fuel heating and cavitation erosion location indicators occurring during the opening and closing periods of the needle valve inside a five-hole common rail Diesel fuel injector are presented. These have been obtained using an explicit density-based solver of the compressible Navier-Stokes (NS) and energy conservation equations; the flow solver is combined with two thermodynamic closure models for the liquid, vapour and vapour-liquid equilibrium (VLE) property variation as function of pressure and temperature. The first is based on tabulated data for a 4-component Diesel fuel surrogate, derived from the Perturbed-Chain, Statistical Associating Fluid Theory (PC-SAFT) Equation of State (EoS), allowing for the variation of the physical and transport properties of the fuel with the local pressure and temperature to be quantified. The second thermodynamic closure is based on the widely used barotropic Equation of State (EoS) approximation between density and pressure only and neglects viscous heating. The Wall Adapting Local Eddy viscosity (WALE) LES model was used to resolve sub-grid scale turbulence while a cell-based mesh deformation Arbitrary Lagrangian–Eulerian (ALE) formulation is used for modelling the injector's needle valve movement. Model predictions are found in close agreement against 0-D estimates of the temporal variation of the fuel temperature difference between the feed and hole exit during the injection period. Two mechanisms affecting the temperature distribution within the fuel injector have been revealed and quantified. The first is ought to wall friction-induced heating, which may result to local liquid temperature increase up to fuel's boiling point while superheated vapour is formed. At the same time, liquid expansion due to the depressurisation of the injected fuel results to liquid cooling relative to the fuel's feed temperature; this is occurring at the central part of the injection orifice. The spatial and temporal temperature and pressure gradients induce significant variations in the fuel density and viscosity, which in turn, affect the formed coherent vortical flow structures. It is found, in particular, that these affect the locations of cavitation formation and collapse, that may lead to erosion of the surfaces of the needle valve, sac volume and injection holes. Model predictions are compared against corresponding X-ray surface erosion images obtained from injector durability tests, showing good agreement.

1. Introduction

Global actions for mitigating the impact of transportation on climate change have pushed governments and professional bodies to target an up to 20% reduction in CO_2 emissions and further limitation of particulate matter mass and NOx from heavy-duty Diesel, marine and aviation engines [1]; such combustion systems are responsible for about 2/3^{rds} of total liquid fossil fuels utilisation in transportation. To achieve today's and future emission standards, injection pressures beyond 200 MPa and multiple injections strategies are required, resulting into liquid jet velocities of the order of 700 m/s [2], as they improve mixing and combustion [3]. At such conditions, the Reynolds and liquid-phase Mach numbers in the nozzle orifices are of the order of 30,000 and around 0.7, respectively; thus, flow is turbulent and compressible, while depending on nozzle hole geometry and needle valve motion, phase-change (cavitation) is typically occurring. On one hand, cavitation collapse could remove surface deposits [4, 5–7] and enhance primary jet break

* Corresponding author:
E-mail address: m.gavaises@city.ac.uk (K. Kolovos).

https://doi.org/10.1016/j.jaecs.2021.100037
Received 8 December 2020; Received in revised form 14 June 2021; Accepted 17 June 2021
Available online 23 June 2021

Nomenclature

English Symbols

A	Surface
a	blending coefficient
B	liquid stiffness/elasticity
C	Speed of sound
C_1	Acoustic impedance
C_d	Discharge Coefficient
cp	Heat capacity
e	Internal energy
E	Total energy
h_0	Total Enthalpy
k	Thermal conductivity
L_c	Characteristic length
M	Mach number
n	Liquid-dependent constant
n	Surface normal vector
p	Pressure
Re	Reynolds number
s	entropy
S_t	Strouhal number
T	Temperature
t	Time
u	Velocity vector
$\mathbf{u_g}$	Grid velocity vector
$\mathbf{u_r}$	Relative velocity vector
V	cell volume
v_f	Vapour Volume Fraction

Greek Symbols

λ_g	Taylor length scale
μ	Dynamic viscosity
ρ	Density
τ	Stress tensor

Subscripts

eff	effective
f	face
in	inlet of injector
L	Liquid
out	exit of the orifice
S	Isentropic
sat	saturation
t	Turbulent

Abbreviations

ALE	Arbitrary Lagrangian–Eulerian
EoS	Equation of State
HEM	Homogenous Equilibrium Model
LES	Large Eddy Simulation
NS	Navier-Stokes
PC-SAFT	Perturbed Chain Statistical Associating Fluids Theory
PVRS	Primitive Variable Riemann Solver
R-P	Rayleigh-Plesset
SCL	Space Conservation Law
URANS	Unsteady Reynolds-averaged Navier–Stokes
VLE	Vapour Liquid Equilibrium
WALE	Wall Adapted Large Eddy

up [8–11] during nominal operating conditions; on the other hand, cavitation collapse could cause material erosion [12, 13], and as a result, affects the durability of various components of the fuel injection equipment; see selectively [14–17]. The violent change in the cavitation cloud volume during collapse causes pressures and temperatures that may even exceed 1 GPa and thousand degrees Kelvin, respectively [18]. Experiments on cavitation in Diesel injection systems have been reported as early as in the '50s [19]; different nozzle geometries have been utilised to reveal its effect on the structure of the injected liquid jets qualitatively [20]. Advanced experimental techniques, such as laser-pulsed light transmission measurements give information about the fluid density and pressure values under overall stationary, highly turbulent and cavitating flow conditions [21]. Shadowgraph Schlieren imaging [22,23] applied to cavitating flows in generic geometries can reveal information for the flow, with pressure waves generated during bubble collapses. Moreover, the understanding and identification of the interaction between turbulence and vortex [24] or string cavitation [25] and their influence on jet and spray characteristics is necessary in order to understand the subsequent air-fuel mixing.

Detailed numerical studies of multi-phase flows in various fuel injectors have been presented since the '90s by solving the incompressible unsteady Reynolds-averaged Navier–Stokes equations (URANS), see for example [25–27]. The strong correlation between internal nozzle flow, string cavitation and primary spray atomization was shown in [28] while the recent works of the authors have shown the influence of injector valve movement during the opening, closing and dwell time of the needle valve [29–32]. Further studies analysed cavitating flows using high-speed digital imaging to capture the instantaneous spatial and temporal characteristics of geometric as well as string cavitation structures [33, 34]; more recent studies employing X-rays [35–37] have provided quantitative data for the cavitation volume fraction, which allows thorough validation of the relevant models. The μm-scale of injectors makes experimental flow characterization challenging. Experiments of erosion damage can provide data about the locations of high structural stresses, which could be linked to cavitation; but they do not produce insight to all features of the underlying flow and thermodynamic conditions needed for the optimization of the performance of the injector. Along the lines of these recent developments, the prediction of cavitation erosion has been also the subject of extensive research. Indeed, the μm-scale of injectors makes experimental flow characterization challenging. Experiments of erosion damage can provide data about the locations of high structural stresses, which could be linked to cavitation; but they do not produce insight to all features of the underlying flow and thermodynamic conditions needed for the optimization of the performance of the injector. In [1,2] and [38,39] a methodology employing flow solvers of the RANS equations has been proposed for cavitating flows; this was found capable of predicting the flow regions of bubble collapse and the potential aggressiveness to material damage. In [40] cavitation was modelled with the use of a barotropic Homogenous Equilibrium Model (HEM) making it suitable for erosion prediction inside a high-pressure fuel pump. In [41] and [42] the impact of the large vortical structures within the nozzle flow and the interaction with incipient and developed cavitation in multi-phase flows was assessed, highlighting the necessity of employing LES to resolve such flows; this was combined with both a barotropic and a mixture model for simulating cavitation. Multi–phase CFD simulations considering flow compressibility can capture the pressure waves generated by collapsing vapour clouds and their impact on nearby surfaces. One of the first studies analysing compressibility effects and wave dynamics in fuel injectors is [43], where a density-based solver of the 3D inviscid Navier–Stokes equations was used. Furthermore, a pioneering investigation of cavitation dynamics and erosion in microchannels was [44], examining different geometries of square orifices, resembling the injection orifice of an actual injector. The focus of the investigation was the demonstration of the potential of barotropic type cavitation models in predicting vapor distribution and erosion locations. In [45] the

turbulence structure was analysed with emphasis put on the interaction between cavitation and coherent flow motion. The numerical work of [46] on Diesel injectors involves compressibility effects, injection to non-condensable gas and an immersed boundary/cut-cell method for handling the needle motion, compressibility of liquid, vapour and non-condensable gases. The authors have achieved an impressive simulation of a complete 9-hole Diesel injector, including injection in air, aiming to study the influence of cavitation and the transient effects of the needle on the emerging jets. The study of [47] confirms the importance of considering local pressure in the improved form of the Rayleigh–Plesset (R-P) equation and illustrates the influence of the liquid compressibility for cavity modelling and appropriate capturing of the collapse pressure. In [48] a fully compressible four-equation model for multicomponent two-phase flow solver, coupled with a real-fluid phase equilibrium model employing the Peng-Robinson (PR) EoS for each phase, is used to demonstrate its capability in predicting phase change effects in simplified shock tube cases and orifices. In [49] the flow inside the same heavy-duty Diesel injector as the one studied in the present work has been performed. In this past work of the authors, the needle valve motion, compressibility and turbulence effects have been considered utilising a pressure-based solver. The recorded pressure peaks obtained have been correlated with the erosion development as identified from X-ray scans of used injectors. Validation of the numerical method and cavitation model was performed in, where X-ray CT scans confirmed the predictions of 3D volumetric cavitation distribution and erosion locations. LES with the employed cavitation erosion model was found able to predict the relevant flow and cavitation aggressiveness features with satisfactory accuracy. More recent works [50–53], have employed a two-fluid model on the simulation of cavitation, erosion and atomization effects of sprays; the overall performance of such models relative to mixture models was assessed revealing little differences for the flow regimes examined. Also, such two-fluid models have been employed for investigating the spray formation of various fuels, including alternative bio-derived variants [54].

Another group of investigations employs the Homogeneous Relaxation Model (HRM), as a mass transfer model, to capture phase change effects. The idea behind the model is to relax the metastable liquid state to reach an equilibrium as liquid/vapor mixture in a finite and often user-calibrated, time-scale. Applications involve flashing where the model was initially conceived, but over time, was adapted for cavitation as well [55]. Further works in the field of fuel injection involve [56], where the authors analyse transient phenomena of needle opening or needle closing with Large Eddy Simulation (LES), as well as the resulting atomisation patterns, in single hole or multi-hole diesel injectors of the Engine Combustion Network (ECN) database. Since then, the HRM model has been used for a variety of applications, including marine injectors for industrial RANS simulations [57] and attempts to devise an erosion metric criterion have also recently performed [58], whereas it has proven to have decent agreement against X-ray densitometry of the spray [59] or the internal flow [60].

For the sake of completeness, it is also worth mentioning a number of recent works employing HEM models, focusing on cavitation and sprays at transcritical and supercritical conditions of ECN Spray-A, using LES and real fluid thermodynamics (Peng-Robinson Equation of State) [61, 62]. The same methodology has also been used to detect cavitation in internal injector flows [63,64]. However, these investigations did not involve any attempt to describe erosion.

Despite their complexity, most aforementioned investigations have ignored viscous heating effects, or at least, did not explicitly discuss about them. However, the flow during the discharge of the fuel is characterized by strong velocity gradients, which induce wall friction and consequently, can result to significant fuel heating. Only limited number of works address fuel heating/cooling and phase-change in high pressure Diesel injectors. The first studies [65–69] from the authors have utilised URANS and have been performed under fixed needle valve conditions; they revealed two opposing processes strongly affecting the fuel injection quantity and temperature; the first one, known as Joule-Thomson effect, is related to the depressurisation of the injected liquid, which results to fuel temperatures even lower than that of the feed. On the other hand, the strong heating produced by wall friction increases significantly the fuel temperature above the boiling point in the near wall regions, where viscous effects are dominant. In follow up works, [70,71] the transient effects owning to the needle motion have shown significant variations in temperature during its opening/closing phase, suggesting that simulations performed at fixed needle lift cannot represent the actual phenomenon. Still, these works have utilised fuel properties from [72] and have not considered the link between cavitation and induced erosion. Recently, new experiments on the properties of diesel fuel at elevated pressures and temperatures have been reported; this has allowed for development and calibration of the PC-SAFT EoS, as

Table 1
Summary of models utilised for resolving the flow in diesel injector nozzles.

Reference	Pressure/density-based	Cavitation model	Needle motion	Properties	Temperature effects	Turbulence model	Erosion
43	Density	HEM	Fixed	Barotropic	No	Inviscid	No
44	Density	HEM	Fixed	Barotropic	No	Inviscid	Yes
63	Density	HEM	Fixed	Real-fluid	No	Inviscid	No
55, 57	Pressure	HRM/ mass transfer	Fixed	Real-fluid	No	RANS k-ε	No
51-53	Pressure, two-fluid	Eulerian, R-P	Fixed	Fixed	No	LES Multi–fluid	Yes
45	Density	HEM	Fixed	Barotropic	No	LES ALDM	Yes
58	Pressure	HRM/ mass transfer	Fixed	Barotropic	No	LES Dynamic 1-eq	Yes
56	Pressure	HRM/ mass transfer	Cut-Cell	Real-fluid	No	LES Dynamic 1-eq	No
41, 49	Pressure	Mass transfer	Fixed & ALE	Barotropic	No	LES WALE	Yes
82	Pressure, two-fluid	Mass transfer	ALE	Fixed	No	RANS k-ε	Yes
31	Pressure	Mass transfer	ALE	Barotropic	No	LES WALE	No
46	Density	HEM	IB/Cut cell	Barotropic	No	LES Implicit	Yes
48	Density	HEM	Fixed	Real-fluid	Yes	Inviscid	No
65-68	Pressure	Lagrangian R-P	Fixed	Real-fluid	Yes	RANS k-ε	No
69	Pressure	Mass transfer	Fixed	Real-fluid	Yes	RANS k-ω SST	No
62,64	Density	HEM	Fixed	Real-fluid	Yes	RANS k-ε, LES	No
99	Density	HEM	Fixed	Real-fluid (PC-SAFT)	Yes	LES WALE	No
61	Density	HEM	Fixed	Real-fluid	Yes	LES Smagorinsky	No
77	Pressure	HEM	Fixed	Real-fluid (PC-SAFT)	Yes	LES WALE	No
81	Pressure	Mass transfer	ALE	Fixed	Yes	RANS k-ε / k-ζ-f	Yes
71	Pressure	Lagrangian R-P	Fixed & ALE	Real-fluid	Yes	RANS k-ε	No
59	Pressure	HRM/ mass transfer	Cut-Cell	Real-fluid	Yes	RANS k-ε	No
Current work	Density	HEM	ALE	Real-fluid (PC-SAFT)	Yes	LES WALE	Yes

reported by the authors in [73–80]; tabulated data have been derived for various fuel surrogates coving the range of properties variation occurring within high pressure fuel injectors and thus allowing for accurate estimation of the effects of fuel property variation to be considered. Still, such effects have not been studied in relation to transient effects caused by the motion of the needle valve.

The presence of a flow regulating valve in fuel injectors poses important complexities in the modelling of the needle/needle seat gap. One of the first methods employed was mesh stretching, were the gap is represented by a fixed cell count which expands and contracts following the needle motion [65–68,81,82]. Unavoidably, this leads to cell quality issues, requiring periodic mesh replacement and field interpolations. Alternative techniques may involve the addition/removal of cell layers beyond a certain lift [49], which avoid entirely the issue of field interpolation. Still, the mesh topology cannot be changed, hence a true needle closure cannot be achieved. This option can be enabled with immersed boundary techniques or cut-cell techniques, which either add source terms to emulate wall presence [29] or actually change the shape/volume of intersecting cells with the wall to introduce the wall presence [46,83].Another alternative that has recently emerged for handling valves is the overset technique [84]; here there are two meshes, one attached to the moving part and another acting as a background. Interpolations and activation/deactivation of cells are performed during mesh motion, to account properly for geometric variations and wall velocity. Further, overset has been also employed in combination with cavitation effects [68]. It has to be noted however, that, despite the flexibility of IB / cut-cell/overset techniques, the needle/needle-seat gap may be represented with very few cells, especially at low lifts.

The mentioned methods for considering the moving computational domain are numerically challenging for simulating the thermal effects for a multiphase compressible flow under 450MPa pressure drop. Higher Reynolds numbers require high grid resolution while higher order schemes may lead to numerical oscillations; this is also needed for the simulation of the boundary layers on surfaces not aligned with the grid lines without unphysical oscillations in the region of sharp corners. The ALE method better resolves these drawbacks. Still, it has some disadvantages: (i) more complex grid generation and more difficult set up to move the computational grid is needed; (ii) during the calculations, large deformations may lead to skewed cells.

For this purpose, the authors have developed and reported recently in [18], an explicit density-based solver flow solver that has been implemented in OpenFOAM; moreover, this solver has been coupled with tabulated fuel property data derived from the real-fluid thermodynamic closure PC-SAFT EoS, as documented by the authors in [73–79] and [85]. As part of the present work, this solver has been further modified to include moving meshes using the ALE approach, as proposed in [86], guaranteeing enforcement of the Space Conservation Law (SCL). Moreover, one of the important features of the developed model is the combination of the Wall Adaptive Eddy (WALE) [87] LES model. In addition to the numerical advancements, the literature review (see Table 1) and to the best of the author's knowledge, there is no relevant simulations reported for cavitation and induced erosion in fuel injectors, while considering variable fuel properties due to temperature/pressure gradients and incorporating transient effects caused by the motion of the needle valve. The developed numerical methodology addresses these phenomena for the first time. Moreover, predictions from this real-fluid thermodynamic closure are also compared to those obtained using the isothermal barotropic model, while results from both simulation approaches are compared against the experimental data reported in [49] for a 5-hole diesel injector.

The paper is structured as follows: first, the mathematical and physical models are presented. Then, the discretization and the thermodynamic closures are analysed followed by the description of the Diesel injector geometry, computational setup and erosion patterns. Then the limitations of the numerical model are discussed, followed by the analysis of the three-dimensional flow-field; this includes analysis of viscous fuel heating and cooling due to depressurisation. Next, the flow-field for the full injection cycle presented while in the final section, the results from the computational analysis are compared with the erosion pattern retrieved from experiments.

2. Mathematical and physical model

The explicit density-based flow solver is based on the works of [18, 49, 88] and [40] but extended here to include moving grids. The mathematical model employs a set of conservation equations governing the fluid motion, re-casted in a form of space conservation law suitable for moving/deforming meshes. The equations with a notation of [86] and written in weak (integral) form given below; bold denotes vector/tensor and italic scalar variables:

- Continuity equation:

$$\frac{\partial}{\partial t}\int_V \rho dV + \int_A (\rho \mathrm{u_r})\cdot \mathrm{n} dA = 0 \tag{1}$$

Here, ρ represents the fluid density, $\mathbf{u_r}$ is the relative velocity of the fluid in respect to the velocity of the moving grid, $\mathbf{u_g}$, defined as $\mathbf{u_r} = \mathbf{u} - \mathbf{u_g}$, $\mathbf{n}$ is the surface normal to the local grid face; V index implies volume integral and A surface integral.

- The momentum conservation equation:

$$\frac{\partial}{\partial t}\int_V \rho \mathrm{u} dV + \int_A (\rho \mathrm{u} \otimes \mathrm{u_r})\cdot \mathrm{n} dA = -\int_A p \mathrm{n} dA + \int_A \tau \cdot \mathrm{n} dA \tag{2}$$

Here, p denotes the fluid pressure and $\boldsymbol{\tau}$ is the viscous stress tensor, defined as:

$$\tau = \mu_{eff}\left[\nabla \mathrm{u} + (\nabla \mathrm{u})^T\right] - 2/3\mu \nabla \cdot \mathrm{u} \tag{3}$$

where μ_{eff} is the effective viscosity of the fluid, including both turbulent (μ_t) and laminar (μ) viscosities.

- Energy conservation equation:

$$\frac{\partial}{\partial t}\int_V \rho E dV + \int_A (\mathrm{u_r} \rho E)\cdot \mathrm{n} dA = -\int_A p \mathrm{u}\cdot \mathrm{n} dA + \int_A \left(k_{eff} \nabla T\right)\cdot \mathrm{n} dA + \int_A (\tau \cdot \nabla \mathrm{u})\cdot \mathrm{n} dA \tag{4}$$

where: E represents the specific total energy of the system, defined as internal energy plus the kinetic energy specific total energy of the system, defined as internal energy plus the kinetic energy, T is the temperature of the fluid and k_{eff} is the effective thermal conductivity of the fluid, including both turbulent (k_t) and laminar (k) components.

- The volume change of cells due to mesh motion can be expressed as:

$$\frac{\partial}{\partial t}\int_V dV + \int_A \mathrm{u_r}\cdot \mathrm{n} dA = 0 \tag{5}$$

For the system closure, expressions for pressure, p, and temperature, T, are necessary to complete equations (2) and (4). These are obtained from the thermodynamic closure, or Equation of State (EoS) employed, which enables to define relations of $T=f(\rho, e)$ and $p=f(\rho, e)$.

2.1. Numerical schemes

The speed of sound in a cavitating flow may vary from O(3) to effectively near zero in the mixture region. Hence, in some parts of the domain the flow can be considered incompressible, whereas in others it is highly compressible. This renders calculations problematic with density based solvers, as they tend to be diffusive in the near incompressible regime, converging to incorrect states [89]. In this work, a hybrid numerical scheme is used, which has been implemented as discussed in [18]; this scheme involves blending of the Mach number (M)

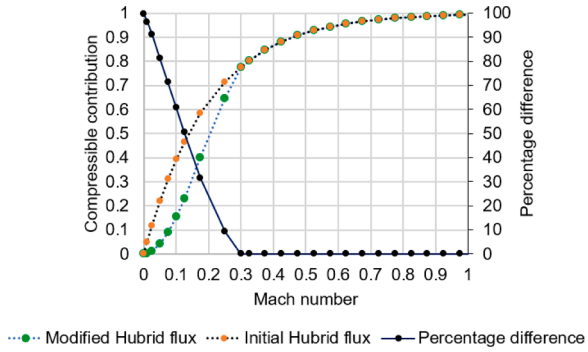

Fig. 1. Illustration of the contribution of the weighted term β (Eq(25) [88]) on the interface pressure as described in Eq(22).

consistent numerical flux of [90], with a compressible variant based on the Primitive Variable Riemann Solver (PVRS - see [91]). The blending is done based on the local Mach number to enhance solver stability; when the Mach number is small, the scheme reverts to the Mach-consistent numerical flux, whereas when the Mach number is large, it switches to the PVRS-variant. Time advancement is performed using a four stage Runge-Kutta method. The allowable step size is usually determined based on the following three factors: absolute (linear) stability, robustness (nonlinear stability) and accuracy as described also in [91]. Moreover during this work it was observed that using a weighted term b Eq(25) [88], for example a blending coefficient α =10 [88], or higher, for both thermodynamic models, the compressible-incompressible contribution at the hybrid flux of the interface pressure Eq(22) [88] influences vortex origin, size, development and reduces or even eliminates vortex cavitation. Also, it was evident that vortices could dissipate in the centre of the nozzle's sac volume, leading to significantly lower amount of overall vapor in comparison with the case where α =1 was used.

$$\beta = 1 - e^{-a\ M_f} \tag{6}$$

The further reduction of the α coefficient does affect the amount of vapor in the injector volume or vortex behaviour attached on solid boundaries or forming closed loops, as expected from the Helmholtz second theorem. The reason is that the high α coefficient influences the momentum numerical flux by rendering the numerical solution much more diffusive. Using an α coefficient very close to zero (e.g. 0.01), the expected vortex behaviour is recovered, but solution stability is adversely affected. Hence, a modification of the blending is proposed here in equation (6) below:

$$\alpha = \alpha_{min} + \left(M_f - M_{min}\right) * \left(\alpha_{max} - \alpha_{min}\right) \ / \ \left(\mathrm{M_{max}} - \mathrm{M_{min}}\right) \tag{7}$$

where $\mathrm{M_f}$, $\mathrm{M_{max}}$ and $\mathrm{M_{nin}}$ denote the Mach number of the surface of the computational cell and its upper and lower limits, respectively; if the Mach number is higher than the corresponding upper limit value, the α coefficient is set equal to this value. In this way, the amount of vapor in the injector volume or the origin and size of vortices is not influenced, while also renders the solver stable especially during the early opening

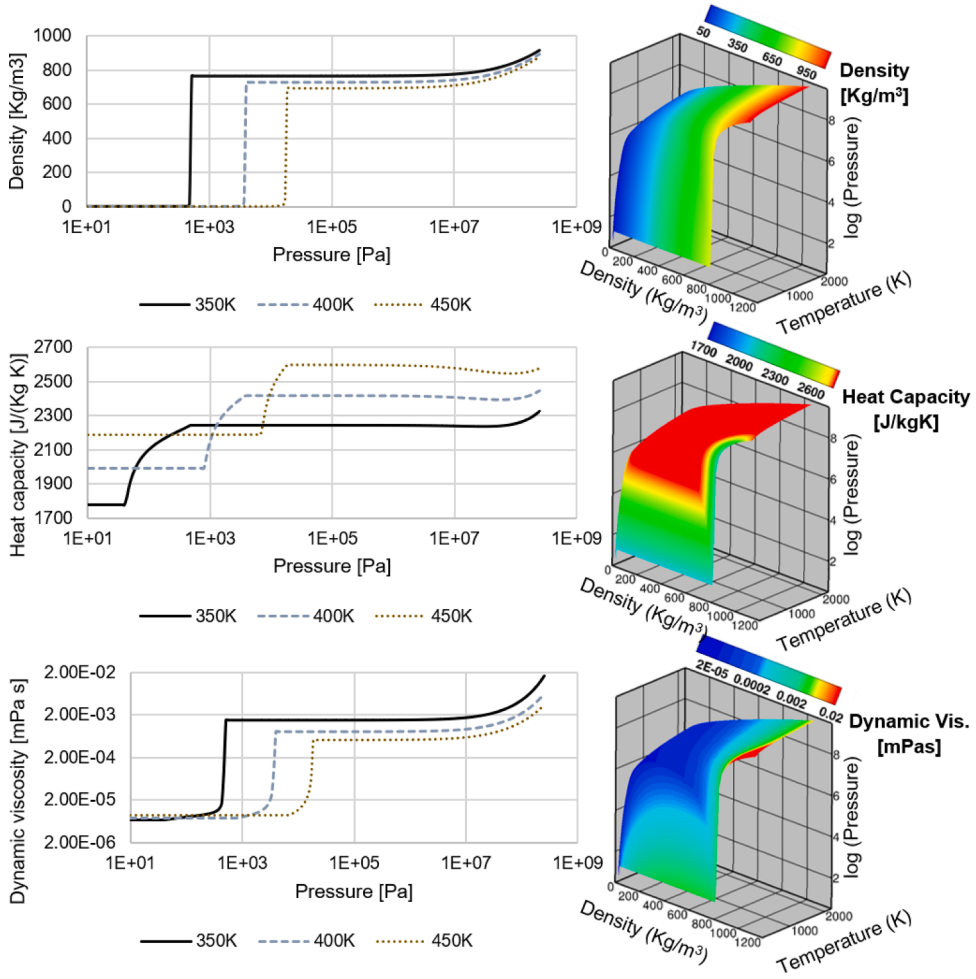

Fig. 2. Illustration of variation of density, heat capacity and dynamic viscosity of the 4-component Diesel fuel surrogate utilised; both two- and three- dimensional plots are shown.

Table 2
Thermophysical properties.

Inlet pressure [10^6 Pa]	180	**Speed of sound Saturation Liquid** [m/s]	950
Density Inlet [kg/m^3]	860	**Saturation density, Vapor**[kg/m^3]	0.1
Speed of sound Inlet [m/s]	1700	**Viscosity, Liquid** [Pa s]	0.000859
Outlet pressure [10^6 Pa]	5	**Viscosity, Vapor** [Pa s]	$7.49*10^{-6}$
Density Outlet [kg/m^3]	733	**Inlet Temperature (Thermodynamic closure 1)** [K]	350
Speed of sound Outlet [m/s]	1070	**Inlet Density (Thermodynamic closure 1)** [kg/m^3]	885.5
Saturation pressure [Pa]	3600	**Inlet Temperature (Thermodynamic closure 2)** [K]	396
Saturation density, Liquid [kg/m^3]	727	**Inlet Density (Thermodynamic closure 2)** [kg/m^3]	863.5

and closing phases. The modified numerical flux based on Eq(25) [88] is shown in Fig. 1;a range of α coefficients from 0.01 (for low Mach number regions) to 5 (for high Mach number regions can be used.

2.2. Thermodynamic closure 1: Thermodynamic properties derived from the PC-SAFT EoS

To address the dependency of physical and transport properties on pressure and temperature, as well as the phase-change characteristics among different fuel components, a technique employing thermodynamic tables is adopted, as described by the authors in [18]; to give an example, the variation of fuel density, dynamic viscosity, heat capacity and conductivity with respect to P-T conditions in the fuel injector is up to 30%, 10^3 %, 40% and 60%, respectively. The advantage of using a table is that it offers flexibility, since a wide range of data can be easily exchanged, while achieving accuracy and low computational cost; this is particularly true when considering complex real-fluid EoS, such as the libraries of NIST [92] or the PC-SAFT EoS [93]. The table is two dimensional, expressed in terms of the decimal logarithm of density and internal energy, over an interval of ρ:0.001 to 1100kg/m^3 and e: -1455kJ/kg to 5000kJ/kg, corresponding to min/max T of 275-2027K and p of 1Pa to 3420 MPa; Maximum rail pressure is 450MPa, and maximum pressures during collapse do not exceed ~1000MPa. Thus, the upper limit used is sufficient; this space is discretised with 500 points for both density and internal energy. Values are stored for all thermodynamic, physical and transport properties, such as pressure (p), temperature (T), enthalpy (h), entropy (s), heat capacity at constant pressure (c_p), speed of sound (c), thermal conductivity (k), dynamic viscosity (μ) and vapour volume fraction (v_f); intermediate values are found using bilinear interpolations.

In combination with this EoS, transport properties such as viscosity and thermal conductivity can be calculated using an entropy scale approach with a good degree of accuracy as reported in [94, 95], while surface tension is modeled using the density gradient theory [96]. Indicatively, the three-dimensional phase diagram derived from the above PC-SAFT EoS for the 4-component surrogate Diesel fuel utilised here, is shown in Fig. 2.

2.3. Thermodynamic closure 2: Barotropic EoS

A two-step barotropic EoS has been used by the authors in [49]; the modified Tait EoS was employed for the liquid phase and the isentropic approximation proposed in [45] was used for the liquid-vapour mixture, as shown by equation (7). In this relationship, C1 is a coefficient that emulates isentropic vaporisation of the liquid; n=7.15 (see [97]) is a liquid-dependent constant while $\rho_{sat.\ L}$ is the saturation density of the liquid at saturation pressure p_{sat}. The properties of the liquid are considered at 396K [49], which is the average temperature between the estimated maximum and minimum temperatures within the computational domain.

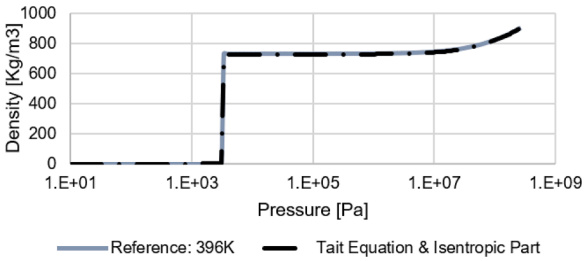

Fig. 3. Utilised density variation with pressure, as predicted by the relevant barotropic fluid EoS.

$$p(\rho)= \begin{cases} (B+p_{sat})\left[\left(\frac{\rho}{\rho_{sat,L}}\right)^n\right]-B, & \rho \geq \rho_{sat,L} \\ p_{sat}+C_1\left[\frac{1}{\rho_{sat,L}}-\frac{1}{\rho}\right], & \rho < \rho_{sat,L} \end{cases} \quad (8)$$

$$B=\frac{\rho C^2}{n}, c=\sqrt{\left(\frac{\partial p}{\partial \rho}\right)_S} \quad (9)$$

Moreover, in equation (7) the coefficient B indicates the liquid stiffness/elasticity. In Table 2, the numerical values for the reference state for computing the Tait parameters are provided. The saturation point properties for the liquid and the vapour phases are provided in Table 2 while Fig. 3 illustrates the variation of density with pressure at the reference temperature of 396K.

3. Description of the examined injector and testing conditions

The simulated geometry is presented in Fig. 4, while specific dimensions of the injector featuring slightly tapered holes are given in Table 3. The injector consists of five orifices, but only the 1/5th of the full injector was simulated, employing symmetry boundary conditions. The computational mesh used consists of a hexahedral block-structured zone, while an unstructured tetrahedral zone is used in the sac volume upstream of the orifice entrance. Mesh motion is performed with a cell-based deformation algorithm, which moves the computational points and cells and stretches them uniformly. The needle lift was initially set at 0.5 μm with 5 cells placed in the needle seat flow passage. The initial flow field was obtained from a steady-state simulation performed at the minimum lift at 0.5 μm in order to have a smoother pressure field from the inlet pressure at the inlet of the injector until the outlet pressure at exit of the orifice. The computational mesh of the sac volume and injection hole, which do not change throughout the simulation, are shown in Fig. 4b and Fig. 4c, respectively. Fig. 5 shows the inlet pressure and needle valve lift, as predicted using the 1-D system performance analysis software, and used as boundary conditions in the CFD simulations. The needle motion is assumed to be in the axial – z direction only; no eccentricity effects are considered. In Table 2, the numerical values for the reference state for the inlet and outlet, respectively, are provided. The simulations were carried out using the WALE model [98]. Based on the cell sizes indicated in Table 3 and the flow conditions, it is possible to make an estimate of the Kolmogorov and Taylor scales of fluid motion for this case, also shown in Table 3. The Taylor length scale gives a characteristic size of inertial scales transitioned to viscous scales and can be used as a resolution target that is respected in the LES. The time step used is 0.5 ns, which corresponds to an acoustic Courant number (CFL) of 0.7 using the speed of sound of liquid; this is also smaller than the Kolmogorov time scale throughout the computational domain.

As shown in Table 4 the injector geometry has been divided in three topologies with different characteristics. The Reynolds number into the injector varies significantly between the needle seat, sac and orifice

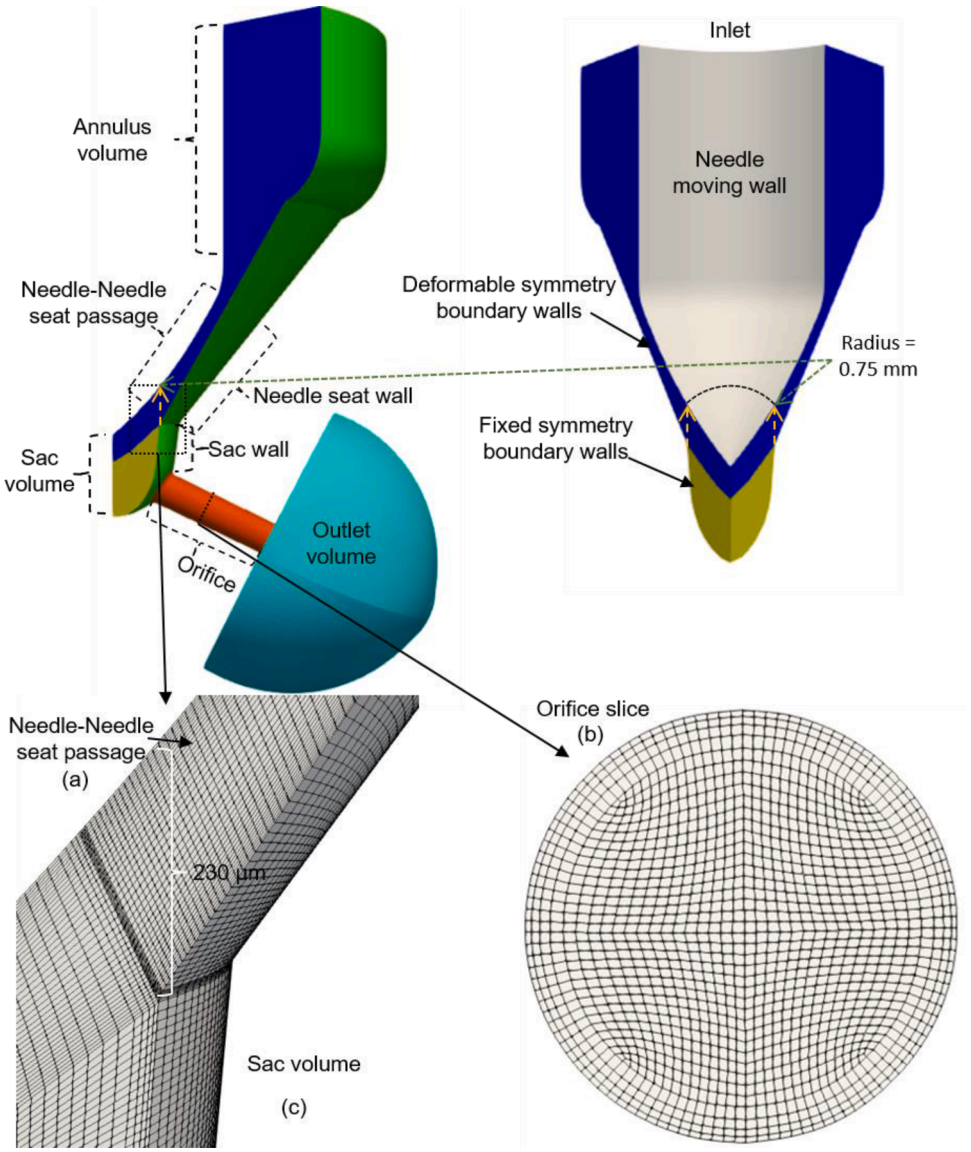

Fig. 4. Naming convention of injector surfaces (top) and 3D view of the computational domain at 70 μm needle lift (bottom).

Table 3
Geometric dimensions of the examined injector.

Max. Needle radius [mm]	1.711	**Orifice diameter Outlet** [mm]	0.359
Orifice length [mm]	1.262	**Sac volume** [mm^3]	1.19
Orifice diameter Inlet [mm]	0.37	**K-factor (D_{in} -D_{out})/10** [μm]	1.1

volume. Given the flow conditions inside the injector the Reynolds number is ~60,000 for the needle and orifice region and ~45,000 for the sac volume. The following values correspond to Taylor length scales, λ_g:

$$\lambda_g = \sqrt{10} Re^{-0.5} L \tag{10}$$

In [99] (Table 2), a mesh independency study showed the differences in the mass flow rate at the exit for the most refined mesh, decreasing the smallest cell sizes to 1.06 μm; therefore, the 1.5 M cells mesh was used for all of the following simulations. The integral quantities of mass and energy balance for every injection pressure, including thermal effects are indicated. The smallest difference of the mass flow at the exit is found for the foremost refined mesh. However, there the difference from the intermediate 1.5M cells mesh is 0.1542% for the 450MPa case; thus,

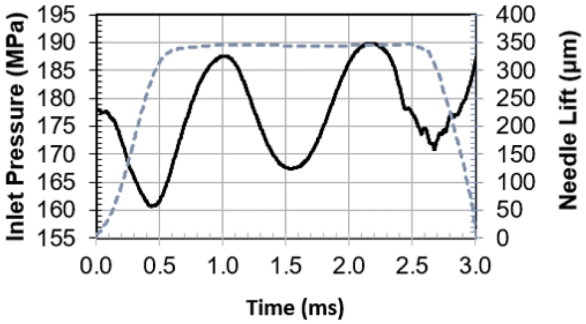

Fig. 5. Injection pressure and needle lift utilised as boundary conditions. The has been predicted using the 1-D system performance analysis model, developed internally by Caterpillar Inc. The input parameters of the 1-D model include engine speed, fuel pressure and temperature, injection duration and regulator back pressure and also incorporate the hydraulic circuit of the endurance bench fuel systems and the electronic control system.

Table 4
Taylor microscale of fluid motion for the injector's different part.

Region	Taylor length scale	Minimum cell size	Kolmogorov time scale
Needle Seat	3 μm	0.1 μm	1.5 ns
Sac Volume	9 μm	7 μm	8 ns
Orifice	4.7 μm	3 μm	2.2 ns

this was used for all following simulations.

4. Injector endurance tests and X-ray erosion patterns testing conditions

Accelerated cavitation erosion durability tests have been performed in an endurance test rig, located at Caterpillar US research and development centre. Endurance testing is conducted for several thousand hours, with injection pressure at 1.1–1.5 times the injector rated operating pressure. The testing fuel is periodically replaced to maintain quality. The injectors are mounted on the head block of the test rig and the injected fuel is collected by the collector block and the rate tube; the downstream pressure adjusted by the pressure regulator at the end of the rate tube. The test rig has a heat exchanger to keep Diesel fuel temperature controlled at 40±1°C in the fuel tank and a computer which collects the data and controls the injection frequency. After the pressurization of the fuel at the nominal pressure of 180 MPa, the fuel reaches 350K, which is the feed temperature at the inlet of the injector. The erosion patterns from the endurance tests have been reported in [49] and they are consistent for all injectors tested at the same time intervals. The needle valve but not the needle seat is affected by erosion as reported in previous work for the so-called 'Design B' in [49], since a deep erosion ring with mean radius of 0.75 mm is visible; for comparison, the larger radius of the nozzle's sac volume is 0.75 mm and the radius of the needle is 1.71mm, as shown in Fig. 4. As reported in [49], the difference between the different Diesel injector designs A and B on erosion on the needle surface is significant. In the nozzle holes, the injector is generally less prone to erosion damage; surface pits have been observed only on the hole's top side. Finally, only minor signs of erosion damage inside the sac volume have been observed, that become apparent after thousands of hours of continuous operation.

5. Limitations and link to previous works

Limitations arising from both the validity of the models themselves utilised and the selection of the specific conditions investigated, include: (1) the dependency/accuracy of the simulations on the equations describing the fuel properties as function of pressure and temperature; (2) the assumption of local mechanical and thermal equilibrium, i.e. vapour and liquid have, locally, the same velocity (no slip) and same temperature, utilised in order to predict the amount of fuel that cavitates; (3) the assumption of adiabatic nozzle walls and (4) the lack of detailed validation against experimental data. A short evaluation of those factors is provided below, before the presentation of the results.

(1) The dependency/accuracy of the simulations on fuel properties as function of pressure and temperature is considered by utilising the PC-SAFT EoS. This EoS [93,94] has been previously used with the Diesel surrogates [100] of this work and compared with experimental results up to 500MPa and 600K for density, viscosity and volatility, [80] with an accuracy of 1.7% for density, 2.9% in volatility and 8.3% in viscosity. Other Diesel properties, such as thermal conductivity, at extreme conditions up to 450MPa and 360K can also be found accurately predicted by PC-SAFT [75, 74, 80] with an accuracy of 3%. It can thus be claimed that the selected EoS is a good compromise for studying such effects in high pressure fuel injectors.

(2) One of the main assumptions in the described methodology is the mechanical and thermodynamic equilibrium between the liquid and the vapour phases. With regards to the mechanical equilibrium assumption, the recent study from the authors using a two-fluid model has confirmed that differences between liquid and vapour velocities are less than 10% and only in localised locations of the flow [51]; they have been found not to affect the overall growth rate and production of vapour. With regards to thermodynamic equilibrium, a metastable, i.e. non-thermodynamic equilibrium, state occurs when the pressure of the liquid drops below the saturation pressure and no vapour is formed, leading to liquid tension, due to the rapid expansion of the liquid [101,102]. The relaxation time of the tensile stresses, i.e. those acting in the metastable state, was numerically estimated to be of the order of 10ns for a vertical tube filled with liquid, impacted vertically and producing an expansion wave of 30MPa [103], however this applies for water in ultra-clean conditions. It is questionable if these scales apply for other fluids and for practical/industrial conditions, where fluids are full of nuclei and surfaces have considerable roughness. Hence, given the uncertainty in nucleation phenomena in industrial applications, where external excitations (turbulence, vibrations), impurities, surface roughness etc., we prefer to avoid ad-hoc assumptions about nuclei content and we prefer to use the HEM model, as it simplifies greatly modelling.

(3) In the absence of information of either the internal (i.e. in contact with the fuel) or the external surface of the injector as well as its detailed geometry and assembly on the cylinder head, any assumption for estimating the heat transfer between the metallic nozzle and the fuel practically is not meaningful. Nevertheless, older studies [70] have estimated the heat transfer based on some gross approximations of those parameters; it clearly suggests that due to the very short time scale of the injection event relevant to the time it takes for wall heat transfer to give an appreciable effect: less than 0.2% variation in the amount of cavitation forming and $0.07\Delta T$ degrees in the mean fuel exit temperature, where stands for the temperature difference when adiabatic walls are considered. Thus, the adiabatic wall assumption is a good approximation for this specific case.

(4) Quantitative experimental data (i.e. vapour volume fraction and velocity flow field) are available only for enlarged nozzle replicas operating at significantly lower pressures. Such validation works have been thoroughly reported from the authors utilising similar models to those reported here. More specifically, the barotropic homogeneous mixture model has been have been validated against the 3D distribution of vapor fraction within the validation uncertainty (±7%, including both numerical and experimental uncertainties) [41, 104]. Further validation has been obtained for the flow field distribution, cavitation frequency shedding and turbulent velocities in the same single-hole injector against high energy X-ray phase contrast imaging (XPCI) measurements for conditions covering a range of cavitation regimes (incipient, fully developed and vortex/string cavitation) [35, 105]. Additionally, validation against Laser Doppler Velocimetry (LDV) measurements has been also reported [41]; this study has also utilised the WALE LES model for turbulence, as it has been proved that can reproduce accurately the turbulent structures found in Diesel nozzles. These studies suggest this model is capable of capturing both incipient and developed cavitation turbulent features. In the present study, the Reynolds number is ~[900-15,000] and thus, it is within the range of applicability of the selected model. As the vaporous core of cavitating vortices has been found to be in the order of 20μm [106], the smallest cell size of ~2μm used is small enough to capture the smallest scales present in the flow that can

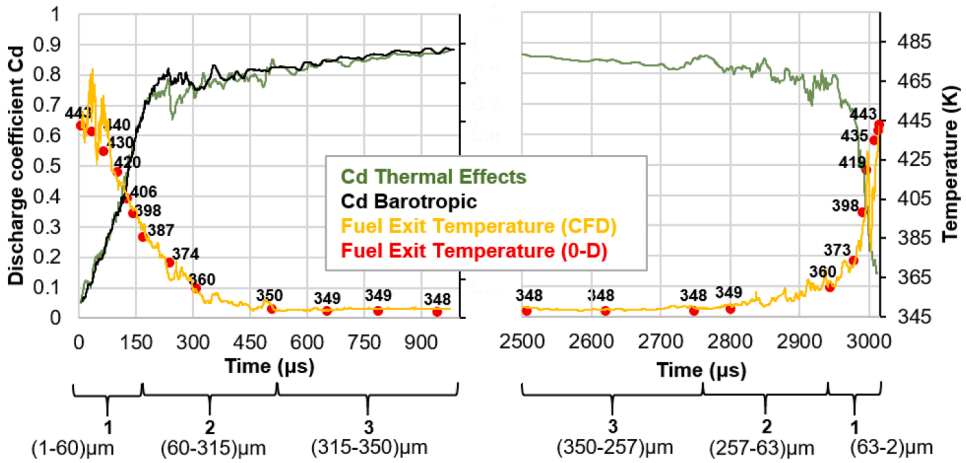

Fig. 6. Nozzle discharge coefficient and fuel exit temperature during the opening (left) and closing (right) phase during injection.

potentially lead to vortex cavitation. Inspection of the calculated flow fields for the tested conditions here suggest that there are no under-resolved vortical structures that may cavitate and significantly influence the obtained results. Moreover, for injection pressures in the range of 180MPa, the same simulated injector geometry was previously validated for predicting cavitation erosion damage utilising the barotropic model. Turning to thermal effects, there are no experiments for real size high pressure Diesel injectors for the temperature variation that can be used for validation. However, a recent study for high-pressure closed loop test bench for fuels temperatures up to 160°C is used to erode micro-channels made of Al 99.0 at a maximum pressure of 500 bar. The temperature of maximum erosion correlates with the temperature dependence of the maximum collapse pressure [107]. Here results will be presented against 0-D predictions of the mean fuel heating up as it discharges through the fuel injector while predictions against the erosion data available are further utilised for the validation of the model.

6. Results

6.1. Comparison against 0-D thermodynamic model predictions

Due to lack of experimental data, a 0-D thermodynamic model is used to estimate the fuel temperature variation between inlet and outlet using equation (10); adiabatic nozzle walls and no work exchange under fixed lift conditions have been assumed, while the generation of turbulence has been ignored. The comparison against the CFD predictions is shown in Fig. 6 as a function of the nozzle discharge coefficient, which is also presented on the same plot; as mentioned earlier, this has been predicted by utilising the two thermodynamic closures. It is reminded that the nozzle discharge coefficient is defined as the ratio between the actual injected fuel mass over the ideal one that would have been obtained without any pressure losses. For fuel injectors, the discharge coefficient changes from zero when the needle valve is closed and takes its maximum value at full lift.

$$T_{out,0D} = T_{out}\frac{(h_{0,in} - h_{0,out})}{h_{0,in}} + T_{out} \tag{11}$$

These estimations have been obtained assuming an initial fuel temperature of 350K. An increase in temperature is observed, particularly during the needle opening and closing periods, where an increase up to 100 degrees is estimated by both the CFD and the 0-D models. Overall, it can be seen that almost identical predictions from both models have been obtained for the mean temperature variation between the inlet and the outlet as function of the needle valve movement. Some differences observed during the very early stages of the needle valve are attributed to transient effects, which are not considered by the 0-D model. Peak values are mainly concentrated into the needle seat passage, starting from its narrowest gap and extending well inside the nozzle's sac volume. Liquid expansion compensates some of the expected fuel heating while cooling is predicted for Cd values higher than 0.8. After the first and second stage of the needle valve opening, the average fuel temperature is very close to the value estimated assuming isentropic

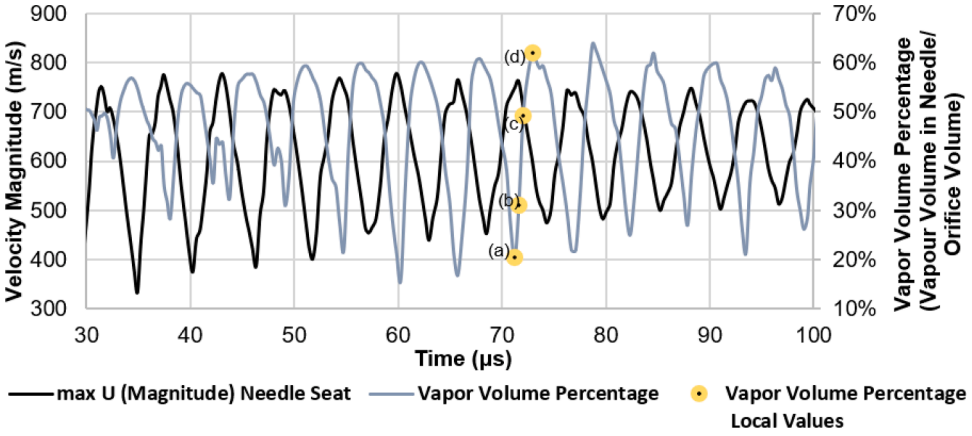

Fig. 7. Temporal evolution of maximum velocity magnitude and vapour volume percentage at the narrowest point at the needle seat passage; lift increase from 12 μm to 35 μm during the plotted time. The points (a) to (d) are indicated as a reference to following figures.

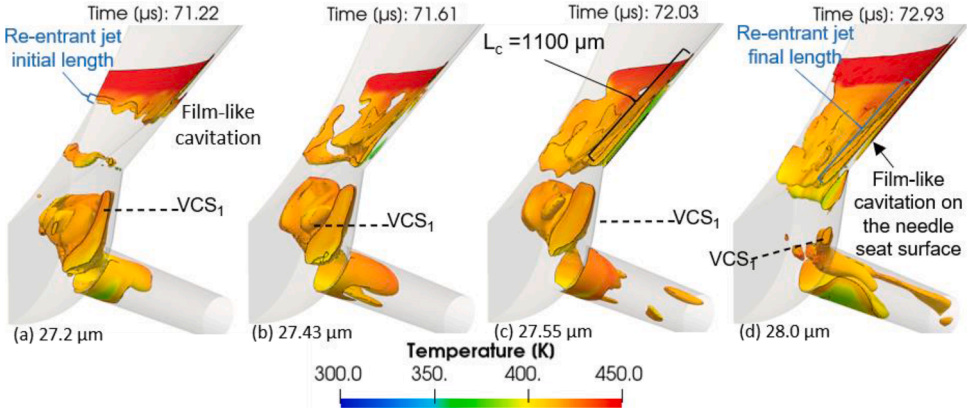

Fig. 8. Snapshots of vapour iso-volume coloured by fuel temperature with vapour volume fraction α = 0.01-1.0 of a representative vapour shedding cycle during the opening of the needle valve from 26.2 μm to 27.2 μm. The selected time instances from (a) to (d) correspond to those indicated in Figure 7.

expansion of the injected fluid, which justifies the use of the barotropic model at sufficiently high needle lifts. Finally, the average fuel temperature seems to be noticeably higher during opening (up to ~470K) when compared to closing (up to ~440K). Finally, the 0-D model seems not to follow the maximum and minimum locals of fuel temperature as predicted by the CFD simulations, especially for the early opening and closing; this is because the 0-D model does not take into account the strong vortex produced into the sac volume that influences the fuel temperature.

6.2. Cavitation development during the opening and closing phases

The opening period of the injection event can be divided into three stages. During the first stage, cavitation appears at the needle seat passage, inside the sac volume and in the nozzle hole. During the second stage, a transition of cavitation from the lower to the upper orifice surface is predicted. Unstable vortex (or string) formations initiate from the needle tip, travel into the orifice inlet and cavitation occurs only in the nozzle hole; sheet cavitation formation is observed at the upper orifice surface and large stable vortical and vapour structures, aligned with the flow direction, dominate. During the third stage, the flow is attached at the vertical wall of sac volume while fully developed cavitation formation is observed at the upper orifice surface. The first stage lasts between 0-150 μs (60 μm), followed by the second stage realized during 150-500 μs (315 μm); and finally, the third stage lasts between 500-985 μs (350 μm). During stage 1, the Cd values are lower than 0.4. During this stage, both thermodynamic closure models predict similar trends for the Cd, vapour volume fraction and turbulence formation. Fig. 7 shows the maximum velocity and the vapour volume formed in the needle seat passage during this time period; a clear vapour formation and shedding pattern can be observed. Vapour formation blocks the liquid fuel through the needle seat passage which results to a decrease in the velocity.

One representative vapour shedding cycle during the opening phase of the needle valve is shown in Fig. 8. The cavitation formation and development at the needle seat passage is closely related to the unsteady recirculation zone and the vortex-cavitation shedding in the sac volume intake or close to vertical sac wall, indicated as VCS_1. Cavitation appears at the needle seat, inside the sac volume and in the orifice, as shown in Fig. 8(a-c). The initial length of the re-entrant jet and the initial length of the detached cavity from the surface increase until they reach their maximum values, as shown in Fig. 8(d). In order to define the frequency of the cavitation cloud shedding, the Strouhal number is calculated based on [108]. As observed from these consecutive instances, vortex cavitation appears within the sac volume; a wall-attached sheet cavity is also observed at the periphery of the nozzle orifice. In Fig. 8(a), the sheet-to-cloud cavitation transition originates.

The mean length of the attached cavity on the needle surface was chosen for the characteristic length L_c, as depicted in Fig. 8(c), while the average velocity U_c is estimated to be ~650m/s. The number of the repeating shedding events during the opening phase is 28 and their duration is ~160μs. Using equation (11), the Strouhal number is ~0.3.

$$St = \frac{fL_c}{U_c} \tag{12}$$

The normalised volume of cavitation formed during the injection

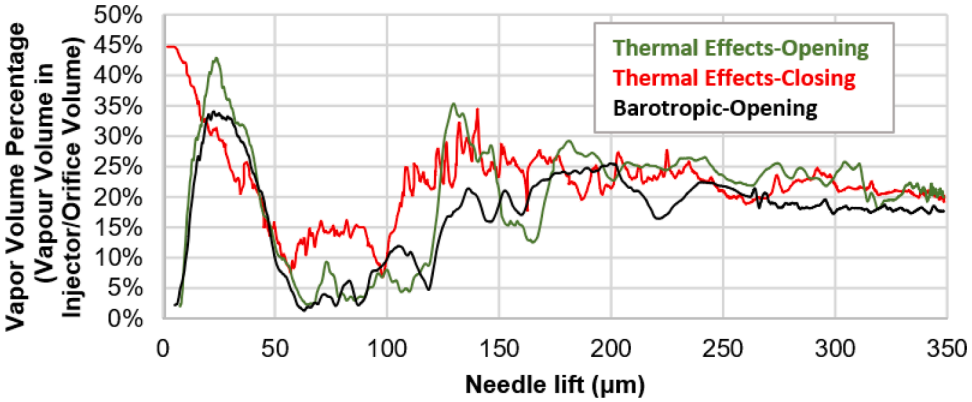

Fig. 9. Vapour volume fraction in the injector volume during the opening and closing phase of the needle valve. Before 150 μs (60 μm) and after 2950 μs (63 μm) the vapour volume is normalised with the sum of the injector's needle seat passage, sac and orifice volumes. In between these times, normalisation only with the orifice volume is performed. It is noted that at zero needle lift the sac volume is 3.1 times larger than the volume of the orifice.

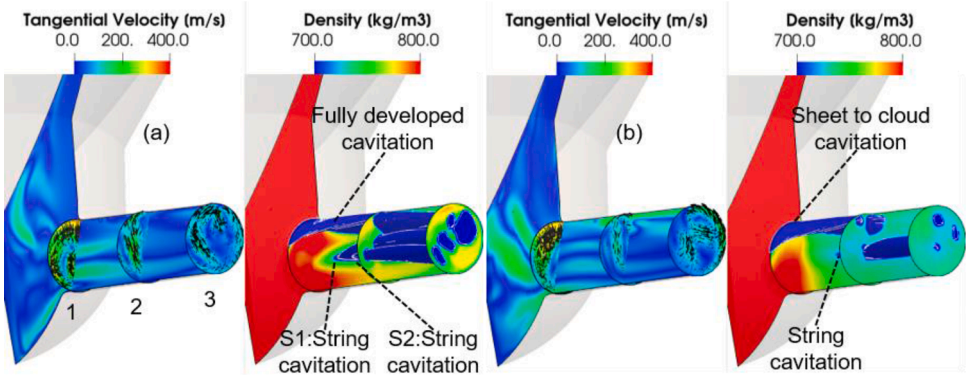

Fig. 10. Instantaneous tangential velocity and density distribution on slices normal to the orifice and at the midplane of the injector, at time instant 248μs (132 μm needle lift) using (a) full thermodynamic model and (b) barotropic model.

period is shown in Fig. 9. During the opening and closing of the needle valve, where cavitation dominates in the needle seat area and the sac volume, the vapour volume is normalised with the sum of the injector's needle seat passage, sac and orifice volumes; while for the period of the injection cycle, where cavitation only appears inside the nozzle hole, normalisation is done using only the volume of the injection hole. During the early opening stages of the needle valve, the amount of the vapour does seem to be noticeably higher for the full thermodynamic closure than that predicted from the barotropic model. This trend also persists over the whole simulation period.

During the early stage of closing, which lasts from 2500 μs (350 μm) to 2750 μs (257 μm) and denoted as 'stage 3' in Fig. 6 and Fig. 9, similar flow and cavitation patterns to those predicted during opening are realised. Differences are realised during the following two stages; 'stage 2' lasts between 2750 μs (257 μm) and 2970 μs (63 μm) followed by 'stage 1' lasting from 2970 μs (63 μm) to 3015 μs (1.6 μm). The amount of cavitation vapour formed shows noticeable differences, up to 12% especially for lower than 35 μm needle lift and up to 15% between 120 and 140 μm needle lift. The amount of the vapour does seem to be noticeably different between opening and closing; calculated differences are 2%-3% for the same needle lift.

6.3. Differences between the thermodynamic closure 1 and 2

Fig. 9 revealed that the vapour volume fraction values vary significantly during the injection event. At some local points the amount of the vapour shows noticeable increase with fluctuations for the full thermodynamic closure case when compared to the barotropic model. This is due to both viscous heating and the formation of different vortical and vapour structures into the sac and orifice volume, forming during the first and the second phases of the needle valve, respectively. As shown in Fig. 10, the comparison between the different thermodynamic models reveals that the velocity, dynamic viscosity and temperature profiles show different trends; this explains the difference in the percentage of vapour volume fraction. The plotting slices into the orifice shown in Fig. 10 are placed at the hole inlet, middle and just before the exit of the orifice. Comparison between Fig. 10(a) and Fig. 10(b) reveals that by neglecting the temperature variations in the case of the barotropic model leads to a more uniform density distribution; as a result, this leads to the suppression of the swirling flow developing inside the nozzle's sac volume. Another reason for the differences between the full thermodynamic and barotropic model is the effect of the baroclinic torque, which cannot be included in a barotropic model, as it is by default zero when the barotropic assumption is utilised. The total derivative of vorticity ω for compressible non-barotropic flow is given, according to [109], by equation 11. The first term on the RHS of the equation is the compressibility term; compressibility increases vorticity, while the following term represents the change in vorticity from vortex stretching and tilting [110]. The third term is the rate change of vorticity due to baroclinicity effect [110]; this term is zero for a barotropic flow, since pressure and density spatial gradients are aligned; the last term represents the change from viscous dissipation.

$$\frac{D\omega}{Dt} = -\omega\nabla\cdot\boldsymbol{u} + \omega\nabla\boldsymbol{u} + \frac{\nabla\rho\times\nabla p}{\rho^2} + \nu\nabla^2\omega \tag{13}$$

As shown in Fig. 10(a), the injector's sac volume and orifice exhibit different temperatures. Some regions are at inlet temperature (350K) or even lower, while others have temperature higher than 390K, due to viscous heating on the needle surface and on the orifice upper wall. As a result, the viscosity field is not uniform; that gives rise to vortex formation, which, in turn leads to formation of cavitation. These strong coherent large-scale vortices underlie on the needle tip surface or the sac volume, causing strong string cavitation that extends into the orifice volume. Furthermore, in Fig. 10(a), three different cavitation structures are evident, which have complex shapes. The first one is the fully developed cavitation at the upper surface of the orifice wall, which is detached from the wall after slice 2. The other two cavitation structures are the two counter rotating vortices indicated as string cavitation S_1 and S_2 in Fig. 10(a). S_1 and S_2 are long and narrow extending to the exit of the injection hole. The S_1 and S_2 are results of the strong swirl of the flow into the sac volume and due to acceleration of the flow as the cross-sectional area of the orifice decreasing.

6.4. Analysis of the flow field and vapour structures

At the first time instant, a highly fluctuating transition from sheet to cloud cavitation, creates a well-established vapour structure into the needle seat passage, as explained in Fig. 8, forming a recirculation zone; next depicted time instant highlights the interaction of vortex cavitation with the flow inside the sac volume up to the needle wall surface, as illustrated in Fig. 11(b), while in Fig. 11(c) the unstable cavitation structure occupies the region close to the sac wall and before the orifice entrance. One part of the fuel is moving backward into the passage close to the needle surface. At the same time, part of the fuel moves parallel to the sac vertical wall. As a result, the upwards flow collides with the high velocity jet, which comes through the needle seat passage at the sac inlet and changes the direction of the jet, as shown in Fig. 11(b-d). The third column shows the detaching cloud sequence, which is a consequence of the vortex shedding. The vortex structure VC_1 gains rotation due to the vortex stretching. The size and circulation may be connected with the sheet length and the vapour cloud detachment [111].

In Fig. 12, focus is placed on the visualisation of the swirl formation [112] and the evolution of vortex cavitation along the orifice length. During the second opening and closing phases, the flow is characterized by sheet-like cavities at the upper wall of the orifice and by aligned vortical vapour cavities into orifice volume. Coherent longitudinal

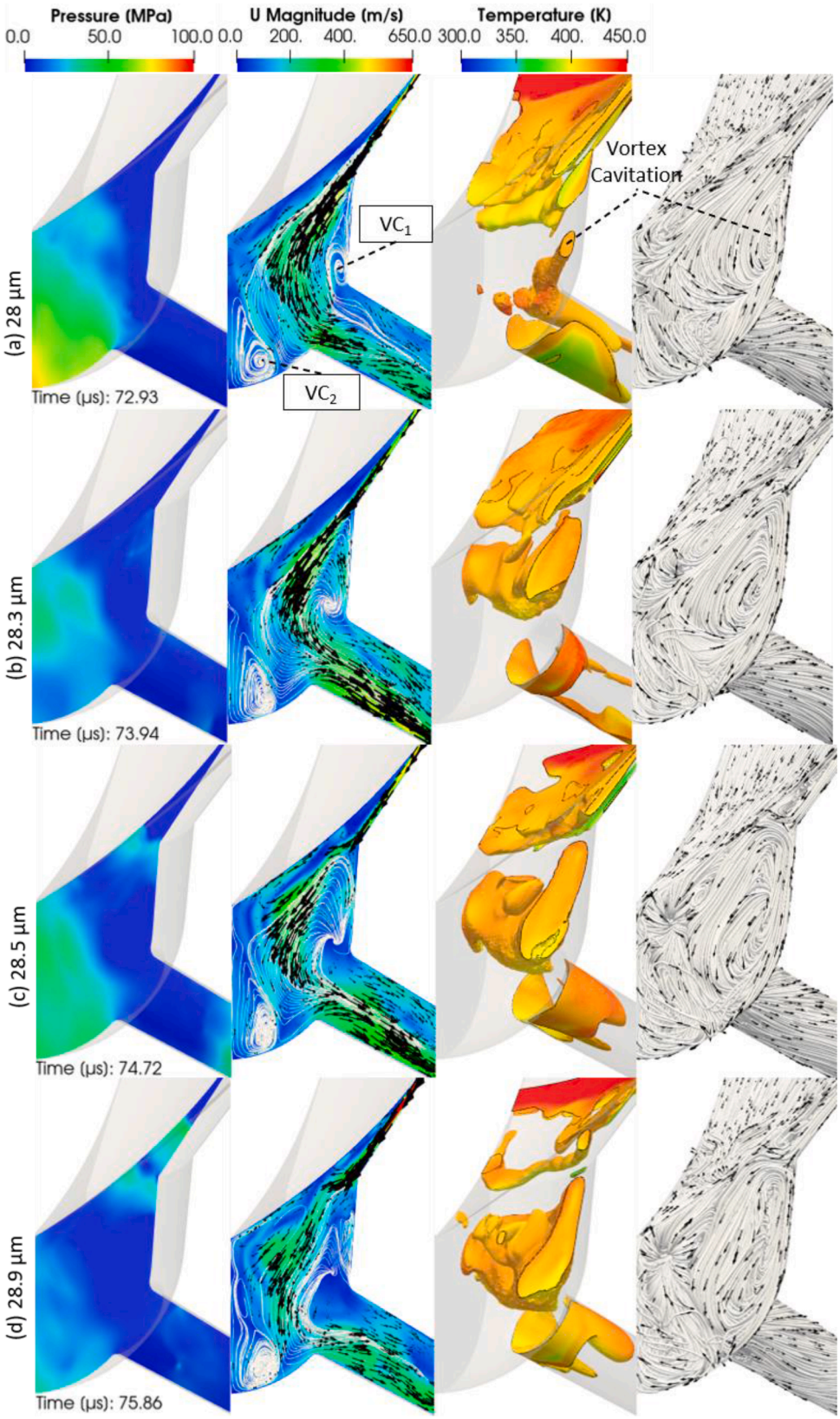

Fig. 11. 3D visualization of the flow during the needle movement from 28 µm to 29.2µm corresponding to; a representative vapour and vortex shedding cycle. Snapshots are presented at time instants (a)–(d) as indicated on the symmetry plane, showing the instantaneous pressure (first column), velocity field (second column); vapour volume fraction coloured with fuel temperature (third column) and flow streamlines (forth column) are also plotted.

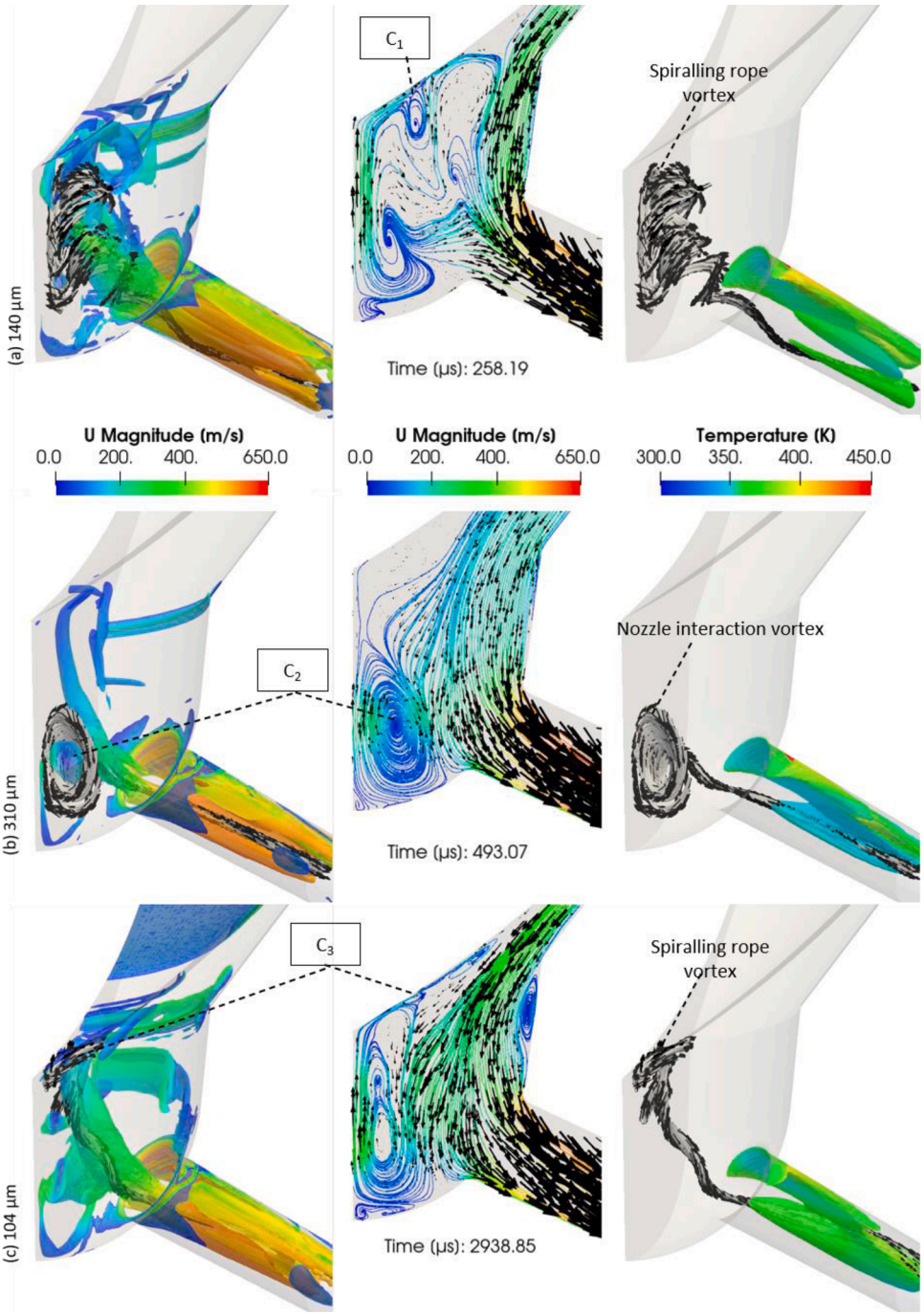

Fig. 12. 3D visualization of a representative vapour and vortex shedding cycle at time instances correspond to (a) 140 µm opening phase, (b) 310 µm, opening phase and (c) 104 µm, closing phase. First column: The iso-surfaces of q criterion with $q = 2.2 \times 10^{12}$ are colored by the velocity magnitude; Second column: flow streamlines at the midplane of the injector coloured by the velocity magnitude; Third column: vapour volume fraction coloured by fuel temperature and flow streamlines.

vortical structures in the sac volume cavitate into the orifice volume. These vortices (C_1 and C_3) originate from the needle tip as depicted in Fig. 12 (a) as strong unstable spiralling tip needle vortex and (c) or from the possible interaction with the other orifices like C_2, Fig. 12(b). This is in agreement with the Helmholtz second theorem stating that vortices cannot terminate in the bulk of a fluid; they must attach on a solid boundary or form closed loops [113]. One significant observation is that at the centre of the initial core of these vortexes, C_1, C_2 and C_3, the Mach number is even lower than 0.1 because the velocity is too low. Due to the acceleration of the fuel into the orifice, the resulting streamwise velocity gradient stretches these vortices, the streamwise vorticity increases and when the pressure drops below the vapour pressure, vortex cavitation appears.

In Fig. 13(a) and (b) the pressure and velocity magnitude fields reveal a different behaviour during the opening and closing phases. During the closing phase, higher fuel mass flow quantities are injected from the nozzle, due to the higher velocity magnitude; the descent of the needle pushes forcefully the fuel mass through the injector and therefore higher Cd is calculated.

Also, the unsteady flow of the fuel jet and the turbulence inside the sac volume create pressure variations in the sac volume which explain the different pressure field between the opening and closing phases at this low lift. At 105 µm needle lift during the closing phase, the downward needle displacement pushes the fuel, having feed temperature, through the needle into the sac volume and then towards the injection hole. The pressure inside the sac volume is ~150 MPa, while during the opening is approximately 5 MPa lower. The differences between the opening and the closing phase progressively disappear near full lift as

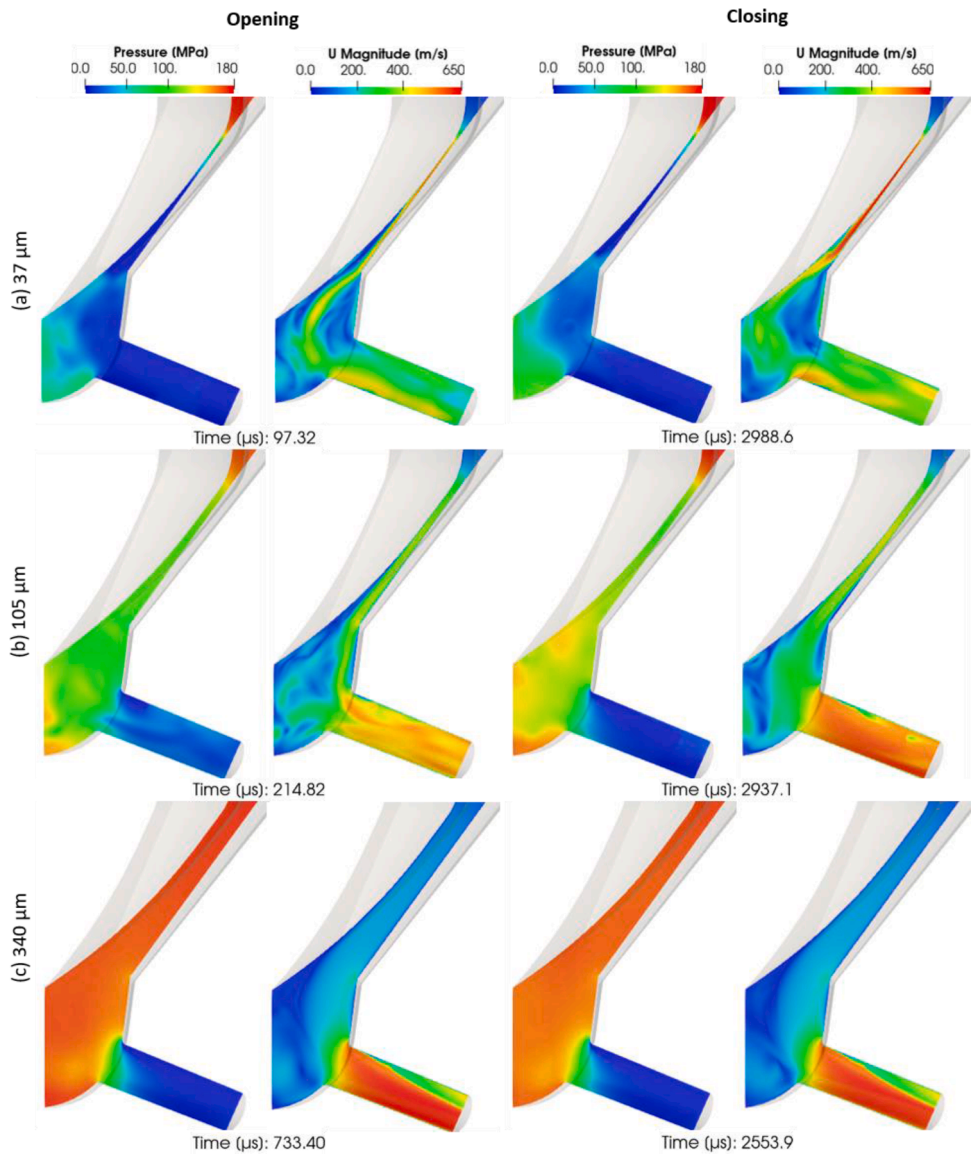

Fig. 13. Snapshots of instantaneous pressure and velocity magnitude at time instances corresponding to (a) 37 µm, (b) 105 µm and (c) 340 µm.

illustrated at 340 µm.

6.5. Analysis of fuel heating and cooling

The fuel heating and cooling is shown on the mid-plane of the injector in Fig. 14. As seen in Fig. 14(a), at 30 µm, the strong viscous heating produced by wall friction leads to higher fuel temperature during the opening of the needle valve than during its closing. At a higher needle lift of 63 µm, shown in Fig. 14(b), both viscous heating and cooling of the fuel take place. Predictions indicate that the liquid fuel temperatures in the needle seat passage are 15K degrees lower than that of the inlet fuel temperature. The cooler fuel jet is more extended during the closing phase than in opening phase. Moreover, during the needle valve closing, the downwards displacement of the needle valve pushes the fuel from the sac volume towards the injection hole, resulting to a decrease of the average fuel temperature at the exit of the nozzle. With regards to the temperature of the vapour, at sufficiently high needle lift, the fuel temperature at the upper surface of orifice can exceed the fuel boiling temperature, resulting to superheated vapour.

Two additional processes affect the temperature of the formed vapour. During cavitation formation, the expansion of the vapour results in temperature decrease, while during vapour collapse, occurring further down inside the hole orifice, significantly higher temperature compared to the surrounding liquid are observed. Moreover, the faster closing phase plays a significant role on the development of different thermal boundary layer into the needle seat passage, as depicted in Fig. 14(b) and (c). This fuel cooling process is related to the de-pressurisation of the fuel; the low pressure due to fuel acceleration and the absence of high-pressure gradients and velocity gradients at the centre of the needle seat passage. As seen, the cooler region in the orifice volume extends and covers a larger region of the orifice volume at higher Cd values. At a higher lift, the strong viscous heating produced by wall friction increases significantly inside the injection hole. The fuel temperature at the upper orifice surface can exceed the fuel boiling temperature. Fig. 14(c)-(d), superheated vapour appears on the injector wall, close to the inlet.

6.6. Analysis of cavitation pattern

Fig. 15(a) shows the vapour volume inside the injector at 15 µm needle lift during both the opening and closing phases; the cloud is additionally presented coloured by the local temperature. Part of the sac

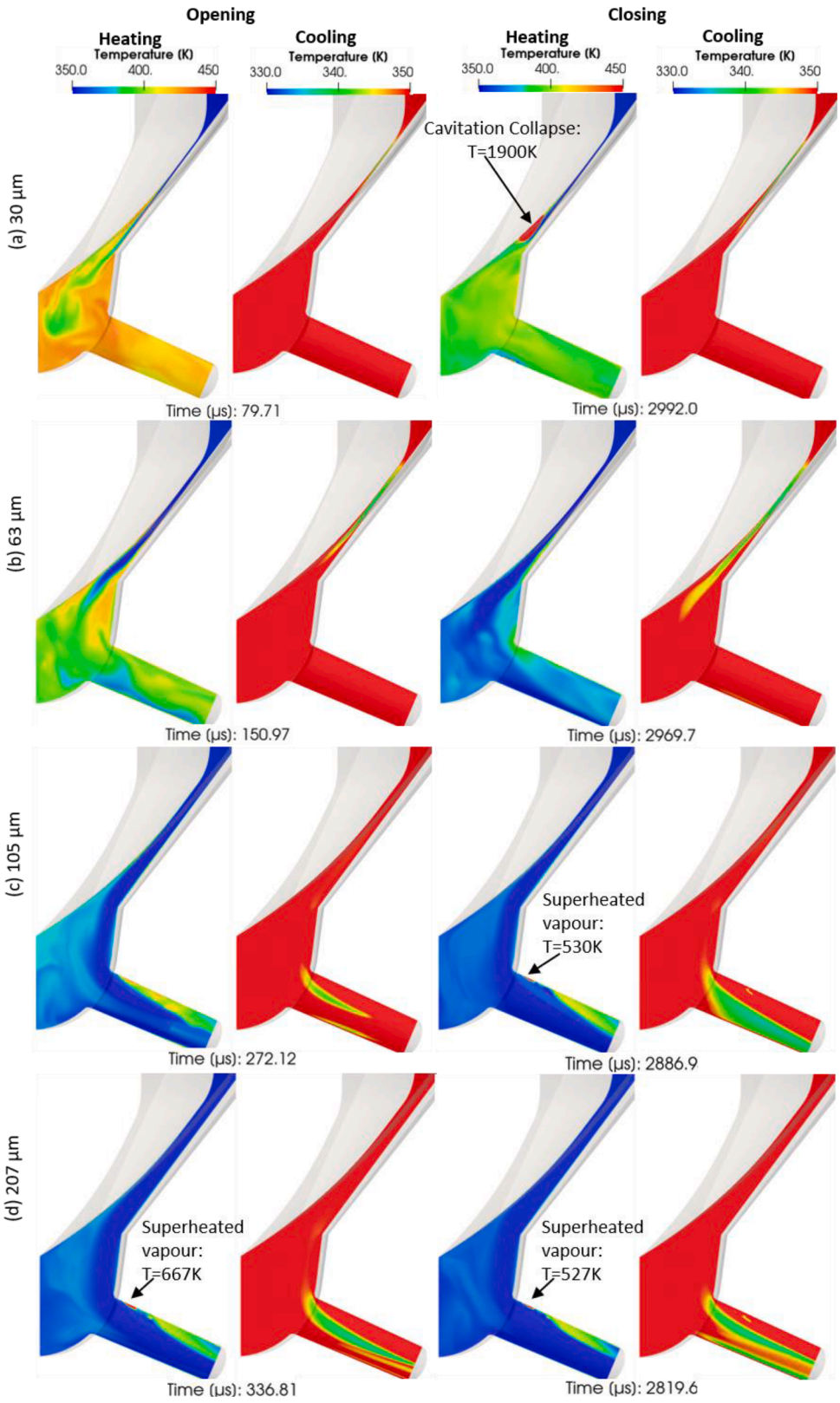

Fig. 14. Snapshots of instantaneous temperature field on the mid-plane of the injector. The time instants correspond to needle lifts (a) 30 µm, (b) 63 µm, (c), 150 µm and (d) 207 µm.

volume is occupied by a symmetric vortex cavitation pattern. The vapour inside the injector at this needle lift during opening is up to 27% of the nozzle's sac volume, while during closing even higher values up to 34% are calculated. At the same time, sheet cavitation is forming in the needle seat passage, while cavitation is also forming inside the injection hole. Until the 214.82 µs and 105 µm lift, cavitation inception forms at the entrance of the orifice, as seen in Fig. 15(b). Before that injection time, cavitation forms close to the lower orifice surface and cavitation

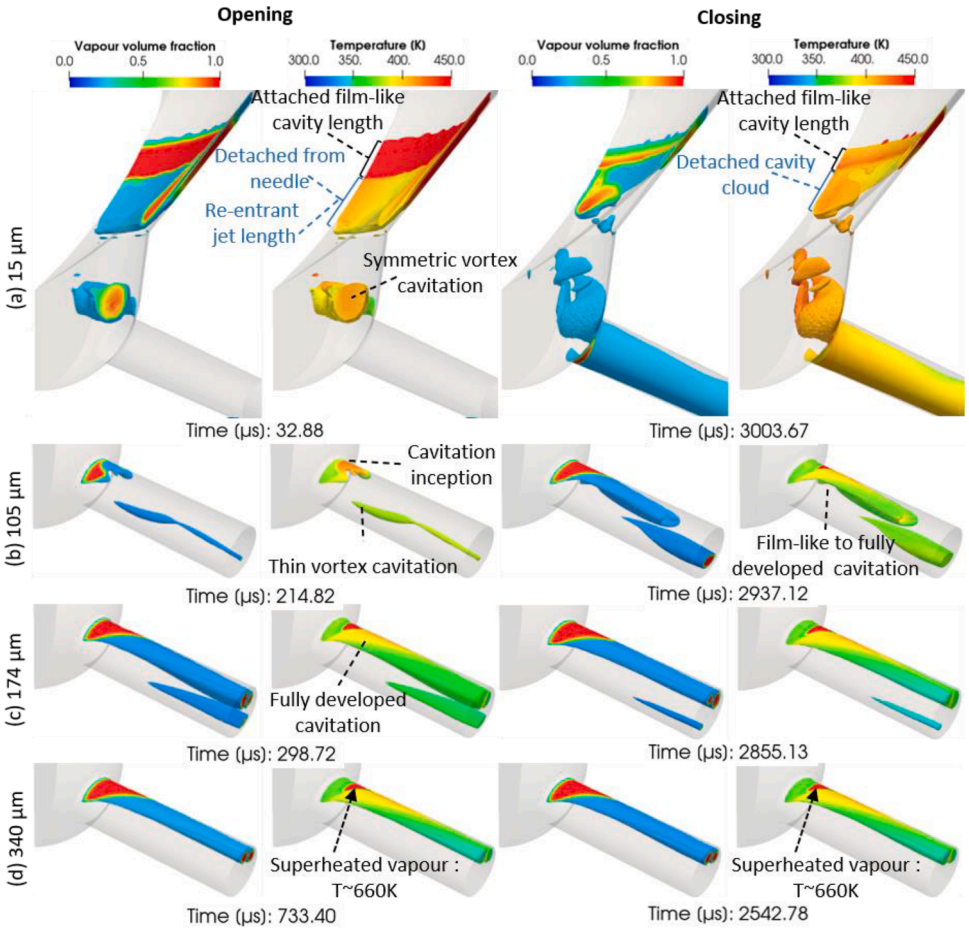

Fig. 15. Snapshots of cavitation formation coloured by the temperature and vapour volume fraction during the opening and closing of the needle valve. The time instants correspond to needle lifts (a) 15 µm, (b)105 µm, (c)174 µm and (d) 340 µm.

structures span in the whole orifice length forming thin string cavitation that may even exit from the orifice. Following, a transition of the cavitation from the lower to upper orifice surface is predicted while during most of the remaining injection time cavitation inside the orifice primarily originates from the top corner of the hole entry, while vortex (or string) cavitation is also observed. Although these patterns are present during both the opening and closing periods, some differences can be observed. In Fig. 15(b) transition from sheet to fully developed cavitation formation is observed at the upper orifice surface and unstable streamwise aligned vortex cavitation structure appear in the orifice volume.

The differences on location, growth and appearance of vapour structures in Fig. 15(b) are related to the higher Cd, around 0.1, predicted during closing and less to the level of heating because the temperature difference is only 20K. At 174 µm lift, coherent cavitation structures appear in the whole nozzle hole, as seen in Fig. 15(c). Fully developed sheet cavitation formation is observed at the upper orifice surface and large scale vortical and vapour structures in the axial direction now dominate the flow. Due to the tapered shape of the nozzle holes, these vortices are further stretched and cause vortex cavitation. The difference on location, growth and appearance of string cavitation in Fig. 15(c) is connected to the higher level of fuel cooling at the centre of the orifice during the closing phase. As seen in Fig. 15(d), at 340 µm lift, the amount of vapour is almost identical during opening; the same applies to the value of the Cd, average fuel temperature and the identical pressure, temperature and velocity magnitude fields.

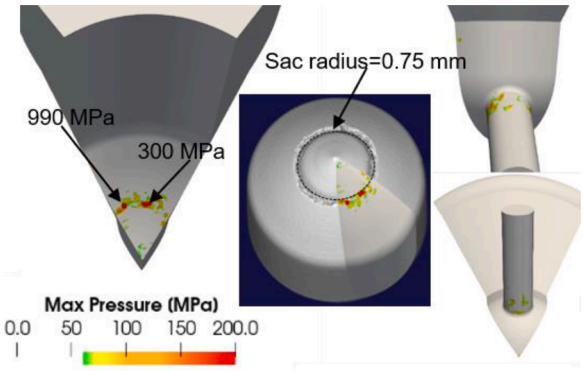

Fig. 16. Spatial distribution of accumulated pressure peaks on the surfaces of the needle valve, sac volume and injection hole; the black line denotes a radius of 0.75 mm where the erosion damage on the needle surface occurs.

6.7. *Analysis of erosion pattern and erosion assessment*

The determination of possible erosion areas during the design process of Diesel fuel injectors is a significant factor for efficient operation and durability. In Fig. 16, the development of the potential erosion due to local maximum accumulated pressure peaks on the injector surfaces is shown. From the experiments a clear pattern is identified with erosion formation on the needle surface in the form of a deeply engraved ring shape. The pressure peaks are predicted in the needle seat passage region between 13 µm and 40 µm. Considering the other surfaces of the

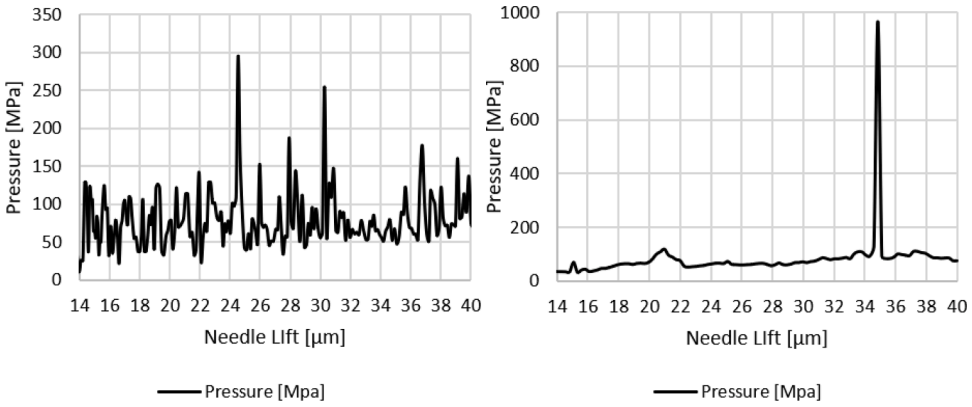

Fig. 17. Peak collapse detector pressures during the needle opening phase (right) and during the needle closing phase (left), recorded during the period when the needle lift moves between 14μm to 40μm.

nozzle, sac is less affected by erosion very close to orifice inlet. In the nozzle holes, the injector is generally less prone to erosion damage, where minor pits on the top side of the injection hole entrance are observed. Moreover, some signs of erosion damage inside the sac volume exist. At the hole inlet, the two locations with potential erosion are predicted very well from the simulation results.

The following Fig. 17 depicts the pressure peaks pattern predicted during the opening and closing at the needle seat region. It is reminded that this small part of the closing phase lasts ~19μs, while the opening lasts ~80 μs. As it can be seen, high frequency local pressure fluctuations take place on the needle seat during the opening period. These fluctuations are the result of the sheet to cloud cavitation transition. However, strongest collapse events are located on the needle surface at the end of the injection phase. High frequency pressure peaks reaching levels of 300MPa and 990MPa during opening and closing, respectively. Based on the combined data of the collapse pressures and the distribution of maximum wall pressures, a significantly higher risk of cavitation erosion on the needle valve surface can be expected during the closing phase. The pressure peaks on the upper orifice surface, starts to form during the transition of cavitation from the lower to the upper orifice surface, as well as during the second stage of the opening, due to cavity shedding developing near this region at the same stages of closing phase. The scale of collapse pressures, like those on orifice entrance, may not be high enough to cause changes to injector material, but the high boiling temperatures, around 660K, with exposure time duration of 2ms at 340 μm lift potentially could potentially contribute to that [114]. The confirmation and noticeable observation for the erosion pattern into the needle seat passage is that erosion is predicted only on the needle surface at radius 0.75mm, in agreement with the experiments.

7. Conclusions

A compressible explicit density-based solver of the Navier-Stokes and energy conservation equations has been employed for simulating the development of cavitation in a five-hole common rail Diesel injector geometry. Two thermodynamic closure models for the liquid, vapour and vapour liquid equilibrium (VLE) property variation as function of pressure and temperature were examined. The first is based on tabulated data for a 4-component Diesel fuel surrogate, derived from the PC-SAFT EoS; the second was based on the widely used barotropic EoS approximation between density and pressure and neglects viscous heating. Model predictions were found in perfect agreement against 0-D estimates of the temporal variation of the mean fuel temperature difference between the injector's inlet and outlet during the injection period. Two mechanisms affect the temperature distribution within the fuel injector. The first is ought to the strong viscous heating produced by wall friction, leading to significant increase of the fuel temperature at the upper orifice surface, where local temperatures can exceed the fuel's boiling temperature and superheated vapour is forming. At the same time, due to Joule -Thomson effect liquid expansion due to depressurisation results to liquid cooling relative to the fuel's feed temperature; this is observed at the central part of the injection orifice. These temperatures gradients induce significant variation of the fuel physical properties locally, which in turn, affect the formed flow structures and in particular the interaction between coherent vortical structures. While the subcooled region into the injector is more evident during the closing phase of the needle valve, the heated region is more pronounced during the opening phase; it is evident that the needle motion affects the thermal boundary layer and possibly the inception and cavity sheet growth and transition, especially at low lifts due to different needle velocity between opening and closing phases. The origin of these vortex cavitation structures was traced into the sac volume and on needle tip surface. Predictions from the full thermodynamic closure model for the peak pressures on the walls of the nozzle were also compared against corresponding X-ray derived surface erosion images obtained from durability tests. Locations of erosion on the surfaces of the needle valve, sac volume and injection holes were in good agreement with the relevant observations.

Overall, the comparison between those two thermodynamic closure models discloses that there are minor differences in the predicted nozzle discharge coefficient but significant differences in the temperature distribution and the vapour volume fraction inside the injector's volume inside the fuel injector as well as the mean injection temperature.

Disclaimer

Acknowledgements

The author(s) disclosed receipt of the following financial support for the research, authorship, and/or publication of the article: This project has received funding from the European Union Horizon-2020 Research and Innovation Programme, Grant Agreement No. 675528.

References

[1] Reitz RD, Ogawa H, Payri R, Fansler T, Kokjohn S, Moriyoshi Y, Agarwal AK, Arcoumanis D, Assanis D, Bae C, Boulouchos K, Canakci M, Curran S, Denbratt I, Gavaises M, Guenthner M, Hasse C, Huang Z, Ishiyama T, Johansson B, Johnson TV, Kalghatgi G, Koike M, Kong SC, Leipertz A, Miles P, Novella R, Onorati A, Richter M, Shuai S, Siebers D, Su W, Trujillo M, Uchida N, Vaglieco BM, Wagner RM, Zhao H. IJER editorial: The future of the internal

combustion engine. Int. J. Engine Res. 2019:3–10. https://doi.org/10.1177/1468087419877990.
[2] Duan L, Yuan S, Hu L, Yang W, Yu J, Xia X. Injection performance and cavitation analysis of an advanced 250MPa common rail diesel injector. Int. J. Heat Mass Transf. 2016;93:388–97. https://doi.org/10.1016/j.ijheatmasstransfer.2015.10.028.
[3] Vera-Tudela W, Haefeli R, Barro C, Schneider B, Boulouchos K. An experimental study of a very high-pressure diesel injector (up to 5000 bar) by means of optical diagnostics. Fuel 2020;275. https://doi.org/10.1016/j.fuel.2020.117933.
[4] Ohl C-D, Arora M, Dijkink R, Janve V, Lohse D. Surface cleaning from laser-induced cavitation bubbles. Appl. Phys. Lett. 2006;89:074–102. https://doi.org/10.1063/1.2337506.
[5] Chahine GL, Kapahi A, Choi J-K, Hsiao C-T. Modeling of surface cleaning by cavitation bubble dynamics and collapse. Ultrason. Sonochem. 2016;29:528–49. https://doi.org/10.1016/j.ultsonch.2015.04.026.
[6] Koukouvinis P, Strotos G, Zeng Q, Gonzalez-Avila S, Theodorakakos A, Gavaises M, Ohl C-D. Parametric Investigations of the Induced Shear Stress by a Laser-Generated Bubble. Langmuir 2018;34:6428–42. https://doi.org/10.1021/acs.langmuir.8b01274.
[7] Zeng Q, Gonzalez-Avila SR, Dijkink R, Koukouvinis P, Gavaises M, Ohl C-D. Wall shear stress from jetting cavitation bubbles. J. Fluid Mech. 2018;846:341–55. https://doi.org/10.1017/jfm.2018.286.
[8] Reitz RD, Bracco FV. Mechanism of atomization of a liquid jet. Phys. Fluids. 1982;25:1730–42. https://doi.org/10.1063/1.863650.
[9] Lin SP, Reitz RD. Drop and Spray Formation from a Liquid Jet. Annu. Rev. Fluid Mech. 1998;30:85–105. https://doi.org/10.1146/annurev.fluid.30.1.85.
[10] Tamaki N, Shimizu M. Enhancement of Atomization of High Viscous Liquid Jet by Pressure Atomized Type Nozzle. In: Proc. Conf. Chugoku-Shikoku Branch. 2002.40; 2002. p. 167–8. https://doi.org/10.1299/jsmecs.2002.40.167.
[11] Sou A, Hosokawa S, Tomiyama A. Effects of cavitation in a nozzle on liquid jet atomization. Int. J. Heat Mass Transf. 2007;50:3575–82. https://doi.org/10.1016/j.ijheatmasstransfer.2006.12.033.
[12] Dular M, Bachert B, Stoffel B, Širok B. Relationship between cavitation structures and cavitation damage. Wear 2004;257:1176–84. https://doi.org/10.1016/j.wear.2004.08.004.
[13] Zhang L, He Z, Guan W, Wang Q, Som S. Simulations on the cavitating flow and corresponding risk of erosion in diesel injector nozzles with double array holes. Int. J. Heat Mass Transf. 2018;124:900–11. https://doi.org/10.1016/j.ijheatmasstransfer.2018.03.086.
[14] Asi O. Failure of a diesel engine injector nozzle by cavitation damage. Eng. Fail. Anal. 2006;13:1126–33. https://doi.org/10.1016/j.engfailanal.2005.07.021.
[15] Brunhart M, Soteriou C, Daveau C, Gavaises M, Koukouvinis P, Winterbourn M. Cavitation erosion risk indicators for a thin gap within a diesel fuel pump. Wear. 2020;442–443:203–40. https://doi.org/10.1016/j.wear.2019.203024.
[16] I.K. Karathanassis, F. Koukouvinis, M. Gavaises, Multiphase Phenomena in Diesel Fuel Injection Systems, in: A.P. Singh, P.C. Shukla, J. Hwang, A.K. Agarwal (Eds.), Simul. Opt. Diagn. Intern. Combust. Engines Curr. Status Way Forw., Springer, Singapore, 2020: pp. 95–126, https://doi.org/10.1007/978-981-15-0335-1_8. https://doi.org/10.1007/978-981-15-0335-1_8.
[17] Koukouvinis P, Mitroglou N, Gavaises M, Lorenzi M, Santini M. Quantitative predictions of cavitation presence and erosion-prone locations in a high-pressure cavitation test rig. J. Fluid Mech. 2017;819:21–57. https://doi.org/10.1017/jfm.2017.156.
[18] Kyriazis N, Koukouvinis P, Gavaises M. Numerical investigation of bubble dynamics using tabulated data. Int. J. Multiph. Flow. 2017;93:158–77. https://doi.org/10.1016/j.ijmultiphaseflow.2017.04.004.
[19] Bergwerk W. Flow Pattern in Diesel Nozzle Spray Holes. Proc. Inst. Mech. Eng. 1959;173:655–60. https://doi.org/10.1243/PIME_PROC_1959_173_054_02.
[20] Guo G, He Z, Chen Y, Wang Q, Leng X, Sun S. LES investigations on effects of the residual bubble on the single hole diesel injector jet. Int. J. Heat Mass Transf. 2017;112:18–27. https://doi.org/10.1016/j.ijheatmasstransfer.2017.04.080.
[21] Iben U, Morozov A, Winklhofer E, Wolf F. Laser-pulse interferometry applied to high-pressure fluid flow in micro channels. Exp. Fluids. 2010;50:597–611. https://doi.org/10.1007/s00348-010-0950-9.
[22] Mauger C, Méès L, Michard M, Azouzi A, Valette S. Shadowgraph, Schlieren and interferometry in a 2D cavitating channel flow. Exp. Fluids. 2012;53:1895–913. https://doi.org/10.1007/s00348-012-1404-3.
[23] Karathanassis IK, Hwang J, Koukouvinis P, Pickett L, Gavaises M. Combined visualisation of cavitation and vortical structures in a real-size optical diesel injector. Exp. Fluids. 2020;62:7. https://doi.org/10.1007/s00348-020-03096-1.
[24] Arndt REA. Cavitation in vortical flows. Annu. Rev. Fluid Mech. 2002;34:143–75. https://doi.org/10.1146/annurev.fluid.34.082301.114957.
[25] Giannadakis E, Papoulias D, Theodorakakos A, Gavaises M. Simulation of cavitation in outward-opening piezo-type pintle injector nozzles. Proc. Inst. Mech. Eng. Part J. Automob. Eng. 2008:1895–910. https://doi.org/10.1243/09544070JAUTO728.
[26] C. Arcoumanis, M. Gavaises, B. Argueyrolles, F. Galzin, Modeling of Pressure-Swirl Atomizers for GDI Engines, in: 1999: pp. 1999-01–0500. https://doi.org/10.4271/1999-01-0500.
[27] Andriotis A, Gavaises M, Arcoumanis C. Vortex flow and cavitation in diesel injector nozzles. J. Fluid Mech. 2008;610:195–215. https://doi.org/10.1017/S0022112008002668.
[28] Gavaises M, Arcoumanis C, Roth H, Choi YS, Theodorakakos A. Nozzle Flow and Spray Characteristics from VCO Diesel Injector Nozzles. In: Whitelaw JH, Payri F, Arcoumanis C, Desantes JM, editors. Thermo- Fluid Dyn. Process. Diesel Engines 2. Berlin, Heidelberg: Springer; 2004. p. 31–48. https://doi.org/10.1007/978-3-662-10502-3_3.
[29] Gavaises Manolis, Koukouvinis Foivos, Gold Martin, Pearson Richard. Mithun Girija Murali, Numerical simulation of fuel dribbling and nozzle wall wetting. Int J. Engine Res. 2021. https://doi.org/10.1177/1468087420985189.
[30] Wang C, Adams M, Luo T, Jin T, Luo F, Gavaises M. Hole-to-hole variations in coupled flow and spray simulation of a double-layer multi-holes diesel nozzle. Int. J. Engine Res. 2020. https://doi.org/10.1177/1468087420963986.
[31] Santos EGomez, Shi J, Gavaises M, Soteriou C, Winterbourn M, Bauer W. Investigation of cavitation and air entrainment during pilot injection in real-size multi-hole diesel nozzles. Fuel 2020;263:716–46. https://doi.org/10.1016/j.fuel.2019.116746.
[32] Gold M, Pearson R, Turner J, Sykes D, Stetsyuk V, de Sercey G, Crua C, Murali-Girija M, Koukouvinis F, Gavaises M. Simulation and Measurement of Transient Fluid Phenomena within Diesel Injection. SAE Int. J. Adv. Curr. Pract. Mobil. 2019;1:291–305. https://doi.org/10.4271/2019-01-0066.
[33] Mitroglou N, Stamboliyski V, Karathanassis IK, Nikas KS, Gavaises M. Cloud cavitation vortex shedding inside an injector nozzle. Exp. Therm. Fluid Sci. 2017;84:179–89. https://doi.org/10.1016/j.expthermflusci.2017.02.011.
[34] Mitroglou N, Gavaises M, Nouri J, Arcoumanis C. Cavitation inside enlarged and real-size fully transparent injector nozzles and its effect on near nozzle spray formation. DIPSI Workshop Droplet Impact Phenom. Spray Investig. Univ. Bergamo Italy. 2011 https://openaccess.city.ac.uk/id/eprint/1507.
[35] Karathanassis IK, Trickett K, Koukouvinis P, Wang J, Barbour R, Gavaises M. Illustrating the effect of viscoelastic additives on cavitation and turbulence with X-ray imaging. Sci. Rep. 2018;8:14968. https://doi.org/10.1038/s41598-018-32996-w.
[36] Mitroglou N, Lorenzi M, Santini M, Gavaises M. Application of X-ray micro-computed tomography on high-speed cavitating diesel fuel flows. Exp. Fluids. 2016;57:175. https://doi.org/10.1007/s00348-016-2256-z.
[37] Brunhart M, Soteriou C, Gavaises M, Karathanassis I, Koukouvinis P, Jahangir S, Poelma C. Investigation of cavitation and vapor shedding mechanisms in a Venturi nozzle. Phys. Fluids. 2020;32:083306. https://doi.org/10.1063/5.0015487.
[38] Koukouvinis P, Bergeles G, Gavaises M. A cavitation aggressiveness index within the Reynolds averaged Navier Stokes methodology for cavitating flows. J. Hydrodyn. Ser B. 2015;27:579–86. https://doi.org/10.1016/S1001-6058(15)60519-4.
[39] Bergeles G, Li J, Wang L, Koukouvinis F, Gavaises M. An Erosion Aggressiveness Index (EAI) Based on Pressure Load Estimation Due to Bubble Collapse in Cavitating Flows Within the RANS Solvers. SAE Int. J. Engines. 2015;8:2276–84. https://doi.org/10.4271/2015-24-2465. https://doi.org/DOI:.
[40] Koukouvinis P, Karathanassis I, Gavaises M. Prediction of cavitation and induced erosion inside a high-pressure fuel pump. Int. J. Engine Res. 2017;19:360–73. https://doi.org/10.1177/1468087417708137.
[41] Koukouvinis P, Naseri H, Gavaises M. Performance of turbulence and cavitation models in prediction of incipient and developed cavitation. Int. J. Engine Res. 2017;18:333–50. https://doi.org/10.1177/1468087416658604.
[42] Papoutsakis A, Theodorakakos A, Giannadakis E, Papoulias D, Gavaises M. LES Predictions of the Vortical Flow Structures in Diesel Injector Nozzles. Warrendale, PA: SAE International; 2009. https://doi.org/10.4271/2009-01-0833.
[43] Sezal IH, Schmidt SJ, Schnerr GH, Thalhamer M, Förster M. Shock and wave dynamics in cavitating compressible liquid flows in injection nozzles. Shock Waves 2009;19:49–58. https://doi.org/10.1007/s00193-008-0185-3.
[44] Skoda R, Iben U, Bosch R, Morozov A, Platz H-L, Mihatsch M, Schmidt S, Adams N. Numerical simulation of collapse induced shock dynamics for the prediction of the geometry, pressure and temperature impact on the cavitation erosion in micro channels. In: WIMRC, 3rd International Cavitation Forum; 2011. https://doi.org/10.13140/2.1.2676.9287. https://doi.org/DOI:.
[45] Egerer C, Hickel S, Schmidt S, Adams N. Large-eddy simulation of turbulent cavitating flow in a micro channel. Phys. Fluids. 2014;26. https://doi.org/10.1063/1.4891325.
[46] Oerley F, Hickel S, Schmidt S, Adams N. Large-Eddy Simulation of turbulent, cavitating fuel flow inside a 9-hole Diesel injector including needle movement. Int. J. Engine Res. 2016;18:195–211. https://doi.org/10.1177/1468087416643901.
[47] Ghahramani E, Arabnejad MH, Bensow RE. A comparative study between numerical methods in simulation of cavitating bubbles. Int. J. Multiph. Flow. 2019;111:339–59. https://doi.org/10.1016/j.ijmultiphaseflow.2018.10.010.
[48] Yi P, Yang S, Habchi C, Lugo R. A multicomponent real-fluid fully compressible four-equation model for two-phase flow with phase change. Phys. Fluids. 2019;31:026102. https://doi.org/10.1063/1.5065781.
[49] Koukouvinis P, Gavaises M, Li J, Wang L. Large Eddy Simulation of Diesel injector including cavitation effects and correlation to erosion damage. Fuel 2016;175:26–39. https://doi.org/10.1016/j.fuel.2016.02.037.
[50] Cristofaro M, Edelbauer W, Koukouvinis P, Gavaises M. Influence of Diesel Fuel Viscosity on Cavitating Throttle Flow Simulations under Erosive Operation Conditions. ACS Omega. 2020;5:7182–92. https://doi.org/10.1021/acsomega.9b03623.
[51] Cristofaro M, Edelbauer W, Koukouvinis P, Gavaises M. A numerical study on the effect of cavitation erosion in a diesel injector. Appl. Math. Model. 2020;78:200–16. https://doi.org/10.1016/j.apm.2019.09.002.
[52] M. Cristofaro, W. Edelbauer, P. Koukouvinis, M. Gavaises, Large Eddy Simulation of the internal injector flow during pilot injection, in: 2018. https://doi.org/DOI:10.1115/1.861851_ch127.

[53] Cristofaro M, Edelbauer W, Gavaises M, Koukouvinis P. Numerical simulation of compressible cavitating two-phase flows with a pressure-based solver. In: Ilass Eur. 28th Eur. Conf. Liq. At. Spray Syst. Universitat Politècnica de València; 2017. p. 896–903. https://doi.org/10.4995/ILASS2017.2017.4629. Editorial.

[54] Battistoni M, Grimaldi CN. Numerical analysis of injector flow and spray characteristics from diesel injectors using fossil and biodiesel fuels. Appl. Energy. 2012;97:656–66. https://doi.org/10.1016/j.apenergy.2011.11.080.

[55] Neroorkar K, Shields B, Ronald O. Grover J, Torres AP, Schmidt D. Application of the Homogeneous Relaxation Model to Simulating Cavitating Flow of a Diesel Fuel. Warrendale, PA: SAE International; 2012. https://doi.org/10.4271/2012-01-1269.

[56] Battistoni M, Som S, Powell CF. Highly resolved Eulerian simulations of fuel spray transients in single and multi-hole injectors: Nozzle flow and near-exit dynamics. Fuel 2019;251:709–29. https://doi.org/10.1016/j.fuel.2019.04.076.

[57] Balz R, Nagy IG, Weisser G, Sedarsky D. Experimental and numerical investigation of cavitation in marine Diesel injectors. Int. J. Heat Mass Transf. 2021;169:120933. https://doi.org/10.1016/j.ijheatmasstransfer.2021.120933.

[58] Magnotti GM, Battistoni M, Saha K, Som S. Development and validation of the cavitation-induced erosion risk assessment tool. Transp. Eng. 2020;2:100034. https://doi.org/10.1016/j.treng.2020.100034.

[59] Xue Q, Battistoni M, Powell CF, Longman DE, Quan SP, Pomraning E, Senecal PK, Schmidt DP, Som S. An Eulerian CFD model and X-ray radiography for coupled nozzle flow and spray in internal combustion engines. Int. J. Multiph. Flow. 2015;70:77–88. https://doi.org/10.1016/j.ijmultiphaseflow.2014.11.012.

[60] Guo H, Torelli R, Rodriguez AB, Tekawade A, Sforzo B, Powell C, Som S. Internal Nozzle Flow Simulations of the ECN Spray C Injector under Realistic Operating Conditions. SAE Int. J. Adv. Curr. Pract. Mobil. 2020;2:2229–40. https://doi.org/10.4271/2020-01-1154.

[61] Yang S, Yi P, Habchi C. Real-fluid injection modeling and LES simulation of the ECN Spray A injector using a fully compressible two-phase flow approach. Int. J. Multiph. Flow. 2020;122:103145. https://doi.org/10.1016/j.ijmultiphaseflow.2019.103145.

[62] Yang S, Habchi C. Real-fluid phase transition in cavitation modeling considering dissolved non-condensable gas. Phys. Fluids. 2020;32:032102. https://doi.org/10.1063/1.5140981.

[63] S. Yang, C. Habchi, P. Yi, R. Lugo, Cavitation Modelling Using Real-Fluid Equation of State, (2018). https://doi.org/10.1115/1.861851_ch44.

[64] Habchi C. A Gibbs free Energy Relaxation Model for Cavitation Simulation in Diesel injectors, ILASS – Europe 2013. In: 25th European Conference on Liquid Atomization and Spray Systems; 2013.

[65] Gavaises M, Theodorakakos A, Mitroglou N. Simulation of heating effects caused by fuel pressurisation at 3000bar in Diesel fuel injectors. In: 8 th International Symposium on Cavitation CAV2012 – Submission No. 216; 2013. https://doi.org/10.3850/978-981-07-2826-7_216.

[66] Salemi R, Koukouvinis P, Strotos G, McDavid R, Wang L, Li J, Marengo M, Gavaises M. Evaluation of friction heating in cavitating high pressure Diesel injector nozzles. Journal of Physics: Conference Series Volume 2015;656. Proceedings of the 9th International Symposium on Cavitation, CAV2015, December 6-10, Lausanne, Switzerland.

[67] Theodorakakos A, Strotos G, Mitroglou N, Atkin C, Gavaises M. Friction-induced heating in nozzle hole micro-channels under extreme fuel pressurisation. Fuel 2014;123:143–50. https://doi.org/10.1016/j.fuel.2014.01.050.

[68] Theodorakakos George Strotos Phoevos Koukou Andreas, Gavaises Manolis. Quantification of Friction-induced Heating in tapered Diesel orifices. In: SIA International Conference on Diesel Powertrains, Int. Congr; 2014.

[69] Payri R, Gimeno J, Martí-Aldaraví P, Alarcón M. A new approach to compute temperature in a liquid-gas mixture. Application to study the effect of wall nozzle temperature on a Diesel injector. Int. J. Heat Fluid Flow. 2017;68:79–86. https://doi.org/10.1016/j.ijheatfluidflow.2016.12.008.

[70] Strotos G, Koukouvinis P, Theodorakakos A, Gavaises M, Bergeles G. Transient heating effects in high pressure Diesel injector nozzles. Int. J. Heat Fluid Flow. 2015;51:257–67. https://doi.org/10.1016/j.ijheatfluidflow.2014.10.010.

[71] Salemi R, Koukouvinis P, Strotos G, McDavid R, Wang L, Li J, Marengo M, Gavaises M. Evaluation of friction heating in cavitating high pressure Diesel injector nozzles. J. Phys. Conf. Ser. 2015;656. https://doi.org/10.1088/1742-6596/656/1/012083. Proc. 9th Int. Symp. Cavitation CAV2015 Dec. 6-10 Lausanne Switz. 656.

[72] Kolev NI. Thermodynamic and transport properties of diesel fuel. In: Kolev NI, editor. Multiph. Flow Dyn. 3 Turbul. Gas Absorpt. Release Diesel Fuel Prop. Springer; 2007. p. 269–302. https://doi.org/10.1007/978-3-540-71443-9_13.

[73] Rokni HB, Moore JD, Gupta A, MHugh MA, Gavaises M. Entropy scaling based viscosity predictions for hydrocarbon mixtures and diesel fuels up to extreme conditions. Fuel 2019;241:1203–13. https://doi.org/10.1016/j.fuel.2018.12.043.

[74] Rokni HB, Gupta A, Moore JD, MHugh MA, Bamgbade BA, Gavaises M. Purely predictive method for density, compressibility, and expansivity for hydrocarbon mixtures and diesel and jet fuels up to high temperatures and pressures. Fuel 2019;236:1377–90. https://doi.org/10.1016/j.fuel.2018.09.041.

[75] Rokni HB, Moore JD, Gupta A, MHugh MA, Mallepally RR, Gavaises M. General method for prediction of thermal conductivity for well-characterized hydrocarbon mixtures and fuels up to extreme conditions using entropy scaling. Fuel 2019;245:594–604. https://doi.org/10.1016/j.fuel.2019.02.044.

[76] Rodriguez C, Rokni HB, Koukouvinis P, Gupta A, Gavaises M. Complex multicomponent real-fluid thermodynamic model for high-pressure Diesel fuel injection. Fuel 2019;257:115888. https://doi.org/10.1016/j.fuel.2019.115888.

[77] Koukouvinis P, Vidal-Roncero A, Rodriguez C, Gavaises M, Pickett L. High pressure/high temperature multiphase simulations of dodecane injection to nitrogen: Application on ECN Spray-A. Fuel. 2020;275:117871. https://doi.org/10.1016/j.fuel.2020.117871.

[78] Rowane AJ, Babu VMahesh, Rokni HB, Moore JD, Gavaises M, Wensing M, Gupta A, McHugh MA. Effect of Composition, Temperature, and Pressure on the Viscosities and Densities of Three Diesel Fuels. J. Chem. Eng. Data. 2019;64:5529–47. https://doi.org/10.1021/acs.jced.9b00652.

[79] Rowane AJ, Mallepally RR, Gupta A, Gavaises M, McHugh MA. High-Temperature, High-Pressure Viscosities and Densities of n-Hexadecane, 2,2,4,4,6,8,8-Heptamethylnonane, and Squalane Measured Using a Universal Calibration for a Rolling-Ball Viscometer/Densimeter. Ind. Eng. Chem. Res. 2019;58:4303–16. https://doi.org/10.1021/acs.iecr.8b05952.

[80] Vidal A, Rodriguez C, Koukouvinis P, Gavaises M, McHugh MA. Modelling of Diesel fuel properties through its surrogates using Perturbed-Chain, Statistical Associating Fluid Theory. Int. J. Engine Res. 2018:1118–33. https://doi.org/10.1177/1468087418801712.

[81] Devassy BM, Greif D, Edelbauer W. Study of Cavitation and 3D Needle Movement due to Erosion in Fuel Injection Nozzles Using Coupled Simulation Tools. In: ILASS-Asia 2016 18th Annu. Conf. Liq. At. Spray Syst. - Asia Chennai India; 2016.

[82] Devassy BM, Edelbauer W, Greif D. Numerical Simulation of the Effect of 3D Needle Movement on Cavitation and Spray Formation in a Diesel Injector. J. Phys. Conf. Ser. 2015;656:012092. https://doi.org/10.1088/1742-6596/656/1/012092.

[83] Koci CP, Fitzgerald RP, Ikonomou V, Sun K. The effects of fuel–air mixing and injector dribble on diesel unburned hydrocarbon emissions. Int. J. Engine Res. 2019;20:105–27. https://doi.org/10.1177/1468087418821827.

[84] Berton A, D'Orrico F, Sideri M. Overset grids for fluid dynamics analysis of internal combustion engines. Energy Procedia 2017;126:979–86. https://doi.org/10.1016/j.egypro.2017.08.240.

[85] Vidal A, Rodriguez C, Koukouvinis P, Gavaises M, McHugh MA. Modelling of Diesel fuel properties through its surrogates using Perturbed-Chain, Statistical Associating Fluid Theory. Int. J. Engine Res. 2020;21:1118–33. https://doi.org/10.1177/1468087418801712.

[86] Demirdžić I, Perić M. Space conservation law in finite volume calculations of fluid flow. Int. J. Numer. Methods Fluids. 1988;8:1037–50. https://doi.org/10.1002/fld.1650080906.

[87] Ducros F, Franck N, Poinsot T. Wall-Adapting Local Eddy-Viscosity Models for Simulations in Complex Geometries. Numer. Methods Fluid Dyn. VI. 1998:293–300. https://doi.org/0952492911.

[88] Kyriazis N, Koukouvinis P, Gavaises M. Modelling cavitation during drop impact on solid surfaces. Adv. Colloid Interface Sci. 2018;260:46–64. https://doi.org/10.1016/j.cis.2018.08.004.

[89] Guillard H, Viozat C. On the behaviour of upwind schemes in the low Mach number limit. Comput. Fluids. 1999;28:63–86. https://doi.org/10.1016/S0045-7930(98)00017-6.

[90] S. Schmidt, I. Sezal, G. Schnerr Professor Dr.-Ing.habil, M. Talhamer, Riemann Techniques for the Simulation of Compressible Liquid Flows with Phase-Transistion at all Mach Numbers - Shock and Wave Dynamics in Cavitating 3-D Micro and Macro Systems, in: 2008. https://doi.org/10.2514/6.2008-1238.

[91] Toro EF. Riemann Solvers and Numerical Methods for Fluid Dynamics: A Practical Introduction. 3rd ed. Berlin Heidelberg: Springer-Verlag; 2009. https://doi.org/10.1007/b79761.

[92] Lemmon E, Huber M. Thermodynamic Properties of n-Dodecane. Energy Fuels 2004;18. https://doi.org/10.1021/ef0341062.

[93] Gross J, Sadowski G. Perturbed-Chain SAFT: An Equation of State Based on a Perturbation Theory for Chain Molecules. Ind. Eng. Chem. Res. 2001;40:1244–60. https://doi.org/10.1021/ie0003887.

[94] Hopp M, Gross J. Thermal Conductivity from Entropy Scaling: A Group-Contribution Method. Ind. Eng. Chem. Res. 2019;58:20441–9. https://doi.org/10.1021/acs.iecr.9b04289.

[95] Lötgering-Lin O, Gross J. Group Contribution Method for Viscosities Based on Entropy Scaling Using the Perturbed-Chain Polar Statistical Associating Fluid Theory. Ind. Eng. Chem. Res. 2015;54:7942–52. https://doi.org/10.1021/acs.iecr.5b01698.

[96] Vinš V, Planková B, Hrubý J. Surface Tension of Binary Mixtures Including Polar Components Modeled by the Density Gradient Theory Combined with the PC-SAFT Equation of State. Int. J. Thermophys. 2013;34:792–812. https://doi.org/10.1007/s10765-012-1207-z.

[97] Ivings MJ, Causon DM, Toro EF. On Riemann solvers for compressible liquids. Int. J. Numer. Methods Fluids. 1998;28:395–418. https://doi.org/10.1002/(SICI)1097-0363(19980915.

[98] Jaberi FA, Colucci PJ. Large eddy simulation of heat and mass transport in turbulent flows. Part 1: Velocity field. Int. J. Heat Mass Transf. 2003;46:1811–25. https://doi.org/10.1016/S0017-9310(02)00484-2.

[99] Vidal A, Kolovos K, Gold MR, Pearson RJ, Koukouvinis P, Gavaises M. Preferential cavitation and friction-induced heating of multi-component Diesel fuel surrogates up to 450MPa. Int. J. Heat Mass Transf. 2021;166:120744. https://doi.org/10.1016/j.ijheatmasstransfer.2020.120744.

[100] C. Mueller, W. Cannella, J. Bays, T. Bruno, K. DeFabio, H.D. Dettman, R. Gieleciak, M. Huber, C.-B. Kweon, S.S. McConnell, W. Pitz, M. Ratcliff, Diesel Surrogate Fuels for Engine Testing and Chemical-Kinetic Modeling: Compositions and Properties, (2016) 1445–1461. https://doi.org/10.1021/ACS.ENERGYFUELS.5B02879.

[101] Caupin F, Stroock AD. The Stability Limit and other Open Questions on Water at Negative Pressure. Liq. Polymorph. John Wiley & Sons, Ltd; 2013. p. 51–80. https://doi.org/10.1002/9781118540350.ch3.

[102] Trevena D. Cavitation and the generation of tension in liquids. J. Phys. Appl. Phys. 2000;17:2139. https://doi.org/10.1088/0022-3727/17/11/003.
[103] Stan CA, Willmott PR, Stone HA, Koglin JE, Liang M, Aquila AL, Robinson JS, Gumerlock KL, Blaj G, Sierra RG, Boutet S, Guillet SAH, Curtis RH, Vetter SL, Loos H, Turner JL, Decker F-J. Negative pressures and spallation in water drops subjected to nanosecond shock waves. J. Phys. Chem. Lett. 2016;7. https://doi.org/10.1021/acs.jpclett.6b00687.
[104] Koukouvinis P, Gavaises M. Simulation of throttle flow with two phase and single phase homogenous equilibrium model. J. Phys. Conf. Ser. 2015;656:012086. https://doi.org/10.1088/1742-6596/656/1/012086.
[105] Karathanassis I, Koukouvinis P, Kontolatis E, Li Z, Wang J, Mitroglou N, Gavaises M. High-speed visualization of vortical cavitation using synchrotron radiation. J. Fluid Mech. 2018;838:148–64. https://doi.org/10.1017/jfm.2017.885.
[106] Reid BA, Gavaises M, Mitroglou N, Hargrave GK, Garner CP, Long EJ, McDavid RM. On the formation of string cavitation inside fuel injectors. Exp. Fluids. 2014;55:1662. https://doi.org/10.1007/s00348-013-1662-8.
[107] Hosbach M, Skoda R, Sander T, Leuteritz U, Pfitzner M. On the temperature influence on cavitation erosion in micro-channels. Exp. Therm. Fluid Sci. 2020;117:110140. https://doi.org/10.1016/j.expthermflusci.2020.110140.
[108] Dular M, Bachert R. The issue of Strouhal number definition in cavitating flow. J. Mech. Eng. 2009;55:666–74. https://doi.org/10.1063/1.3699067. https://doi.org/.
[109] Cecere D, Ingenito A, Giacomazzi E, Romagnosi L, Bruno C. Hydrogen/air supersonic combustion for future hypersonic vehicles. Int. J. Hydrog. Energy. 2011;36:11969–84. https://doi.org/10.1016/j.ijhydene.2011.06.051.
[110] Long X, Liu Q, Ji B, Lu Y. Numerical investigation of two typical cavitation shedding dynamics flow in liquid hydrogen with thermodynamic effects. Int. J. Heat Mass Transf. 2017;109:879–93. https://doi.org/10.1016/j.ijheatmasstransfer.2017.02.063.
[111] Pelz PF, Keil T, Groß TF. The transition from sheet to cloud cavitation. J. Fluid Mech. 2017;817:439–54. https://doi.org/10.1017/jfm.2017.75.
[112] Brennen CE. Hydrodynamics of Pumps. Concepts ETI; 1994.
[113] Batchelor GK. An Introduction to Fluid Dynamics. Cambridge University Press; 1973.
[114] Kim K-H, Chahine G, Franc J-P, Karimi A. Advanced Experimental and Numerical Techniques for Cavitation Erosion Prediction. Springer; 2014.